RADIATION DATABASE FOR EARTH AND MARS ENTRY

Marie-Yvonne Perrin, Philippe Riviere, Anouar Soufiani

Laboratoire EM2C, CNRS UPR 288, Ecole Centrale Paris
92295 Chatenay-Malabry Cedex France

November 17, 2008

ABSTRACT

This lecture presents the general guidelines we have followed to build up an exhaustive and accurate spectroscopic database for radiative transfer in air and CO_2-N_2 plasma applications, including atmospheric entries. This High Temperature Gas Radiation (HTGR) database includes bound-bound atomic, diatomic and polyatomic (in particular CO_2) transitions, bound-free transitions resulting from various mechanisms, and free-free transitions. The covered spectral range is 1000–200,000 cm^{-1} and the targeted maximum temperature is 30,000 K. A particular attention is given to the selection of the most reliable fundamental data (line strengths for atoms and ions, electronic transition moment functions and spectroscopic constants for diatomic molecules, cross sections for continuum radiation), and to accurate prediction of atomic and ion line shapes which are strongly self-absorbed. The spectroscopic database is applied in the last part of this lecture to the simulation of Fire II experiment as an example of earth entry, and to the prediction of a Mars entry simulation. We discuss in these applications the spectral distribution of radiative fluxes from the infrared to the VUV, the effects of optical thicknesses and self-absorption, and the effects of chemical nonequilibrium on continuum radiation.

1 Introduction

During atmospheric entries, the gas heated in the shock layer will emit a radiation that will contribute to the incident flux at the vehicle surface. Different mechanisms are involved which give rise to a complex structure of the emission and absorption spectra. Bound-bound transitions in atoms and molecules will give line spectra. Free-free transitions will contribute to a continuous spectrum. Bound-free transitions will give a continuous spectrum with eventually some structures. The radiative spectral intensity $I_\sigma(\mathbf{u})$ ($\mathrm{W.m^{-2}.sr^{-1}.(m^{-1})^{-1}}$) can be obtained at each point, for each propagation direction $\mathbf{u}$, and each wavenumber σ ($\mathrm{m^{-1}}$) by solving the radiative transfer equation (RTE):

$$\frac{dI_\sigma(\mathbf{u})}{ds} = \eta_\sigma - \kappa_\sigma I_\sigma(\mathbf{u}), \tag{1}$$

where s is the optical path along $\mathbf{u}$, κ_σ is the absorption coefficient ($\mathrm{m^{-1}}$), and η_σ is the emission coefficient ($\mathrm{W.m^{-3}.sr^{-1}.(m^{-1})^{-1}}$). The above equation has been written assuming that scattering by possible solid particles is negligible, otherwise, the propagation directions are coupled by this phenomenon. The RTE requires one boundary condition corresponding to the intensity leaving the wall point which intersects the propagation direction if $\mathbf{u}$ is directed outward this

wall, and zero otherwise. The radiative flux on a surface can be calculated from the intensity following:

$$\mathbf{q}_R = \int_0^\infty d\sigma \int_{4\pi} I_\sigma(\mathbf{u})\, \mathbf{u}\cdot\mathbf{n}\, d\mathbf{u} \tag{2}$$

where $\mathbf{n}$ is the normal to the considered surface, and the amount of power exchanged between the matter and the radiation field per unit volume is given locally by:

$$P_R = \int_0^\infty d\sigma \int_{4\pi} (\eta_\sigma - \kappa_\sigma I_\sigma(\mathbf{u}))\, d\mathbf{u} \tag{3}$$

κ_σ and η_σ are local quantities which depend on the thermochemical states of the emitting and absorbing species. If the medium is at local thermodynamic equilibrium (LTE) at temperature T, κ_σ and η_σ are linked through the Kirchhoff's law:

$$\eta_\sigma = \kappa_\sigma I^0_\sigma(T), \tag{4}$$

where $I^0_\sigma(T)$ is the equilibrium intensity given by the Planck's law:

$$I^0_\sigma(T) = \frac{2hc^2\sigma^3}{\exp(\frac{hc\sigma}{kT}) - 1}, \tag{5}$$

h, k and c being respectively Planck and Boltzmann constants, and the speed of light.

An accurate modelling of radiation is required for several reasons:

- Radiation is currently used in ground experiments and in some flight tests to characterize the state of the medium. These optical measurements are usually done in the visible and UV range, sometimes in the IR and vacuum UV (VUV). It is thus necessary to have data of spectroscopic quality in these spectral ranges.
- For high velocity entries, the radiative flux at the wall can be important and even predominant. To calculate this flux, it is necessary to have a data base which includes all the mechanisms that will contribute to the emission or absorption in a wide spectral range.
- Radiation is an additional energy transport mechanism and can also affect the chemical state of the gaz through emission, photodissociation, photionization , radiative recombination . . . In some situations, it can be necessary to take into account the effect of radiation on the flowfield and to perform coupled calculations of the fowfield and of the radiation field. However solving the RTE is computationally very expensive. To reduce the calculation cost, approximate models of radiative properties can be developed.

There are several computer codes and spectral databases developed for radiation analysis (NEQAIR96 [1], LORAN [2], SPRADIAN [3], MONSTER [4], SPECAIR [5], PARADE [6], HARA [7], GPRD [8]. . .). However some of them are classified, other do not completely satisfy the following requirements:

- Cover a wide temperature range (up to 30000K for entry applications but also for other plasma applications).
- Consequently, cover the whole useful spectral range including infrared and VUV ranges.
- Allow line-by-line calculations with the fine structure of bound-bound atomic and molecular spectra to accurately predict radiative transfer with absorption.

For these reasons, we have developed a database, called HTGR (High Temperature Gas Radiation), for air first [9, 10] using the latest spectroscopic constants and transition probabilities. This database was recently extended to CO_2–N_2 plasmas [11, 12] and the development of some approximate radiative property models is under progress.

In the following we give the guidelines we have followed to build this database. Such developments rely on spectroscopic concepts which are not straightforward. The interested reader is invited to consult specialized books on these concepts. A few examples of application of the database are given. For applications involving local thermal equilibrium, we calculate the populations of the different emitting species from statistical physics. For entry applications under nonequilibrium conditions, we use thermochemical fields calculated by other groups.

2 Database

The database allows to calculate the monochromatic emission coefficient η_σ and the monochromatic absorption coefficient κ_σ for all the radiative processes and species listed in table 1 which are relevant to Earth and Mars entries. Other polyatomic IR data (H_2O and CH_4) have also been developed for combustion applications [13, 14].

Bound-bound transitions	
– atomic species	N, N^+, N^{++}, O, O^+, O^{++}, C, C^+
– diatomic species	N_2, O_2, NO, N_2^+, C_2, CO, CN, CO^+
– triatomic species	CO_2
Bound-free transitions	
– atomic photoionization	N , N^+, O, O^+
– atomic photodetachment	N^-, O^-, C^-
– molecular photoionization	N_2, O_2, NO, C_2, CO, CN
– molecular photodissociation	O_2 Schumann-Runge
free-free transitions	N, N^+, N^{++}, O, O^+, O^{++}, C, C^+
other mechanism	chemiluminescence CO + O

Table 1: Radiative processes taken into account.

2.1 Bound-bound transitions

We consider a radiative transition between bound energy levels u (upper) and l (lower) of a species A. Three mechanisms have to be retained for energy transfer applications: spontaneous emission, absorption, and stimulated emission, corresponding to the following reaction schemes

$$\begin{aligned} A(u) &\rightarrow A(l) + hc\sigma_{ul} && \text{spontaneous emission} \\ A(l) + hc\sigma_{ul} &\rightarrow A(u) && \text{absorption} \\ A(u) + hc\sigma_{ul} &\rightarrow A(l) + 2hc\sigma_{ul} && \text{stimulated emission} \end{aligned}$$

where σ_{ul} is the wavenumber of the emitted/absorbed photon. $hc\sigma_{ul}$ in the above reactions designates the energy of the photon and satisfies

$$hc\sigma_{ul} = E_u - E_l, \tag{6}$$

where E_u and E_l are the energies of the upper and lower levels. Three Einstein coefficients A_{ul}, B_{lu} and B_{ul} associated respectively to the three above radiative mechanisms are usually

introduced, enabling to express the contribution of these bound-bound transitions to the spetral emission and absorption coefficients of the medium at current wavenumber σ according to

$$\eta_\sigma = \sum_{ul} \frac{A_{ul}}{4\pi} hc\sigma_{ul} n_u f_{ul}(\sigma - \sigma_{ul}), \tag{7}$$

$$\kappa_\sigma = \sum_{ul} (n_l B_{lu} - n_u B_{ul}) h\sigma_{ul} f_{ul}(\sigma - \sigma_{ul}), \tag{8}$$

where n_u and n_l designate the population of the upper (u) and lower (l) transition levels, and $f_{ul}(\sigma - \sigma_{ul})$ is the spectral line shape of the transition accounting for Doppler, natural and collisional broadening. Einstein coefficients are intrinsic parameters of the radiating particle and satisfy the relations

$$A_{ul} = 8\pi hc\sigma_{ul}^3 B_{ul}, \tag{9}$$

$$g_u B_{ul} = g_l B_{lu}, \tag{10}$$

where g_u and g_l are the degeneracies of levels u and l. Because of these relations between Einstein coefficients, we need to know only one of them for each transition.

To predict bound-bound absorption or emission spectra, we need to know for all the transitions the line position, σ_{ul}, the strength of the transition, e.g. B_{lu} (in fact we will see in the following that atomic and molecular spectroscopists use different quantities related to B_{lu}), the line shape $f_{ul}(\sigma - \sigma_{ul})$, and of course the thermodynamic state of the medium, i.e. the n_u and n_l values.

In the following, we will discuss only electric dipolar transitions since they are the main contributors to radiative energy transfer. In this case, the absorption Einstein coefficient B_{lu} may be expressed as

$$B_{lu} = \frac{8\pi^3}{3h^2 c} \frac{1}{4\pi\varepsilon_0} \frac{1}{g_l} R_{ul} \tag{11}$$

where the transition moment R_{ul} is obtained from the the dipolar moment operator $\boldsymbol{\mu}$ of the radiating particle according to

$$R_{ul} = \sum_{m_l m_u} \left| \langle l, m_l | \, \boldsymbol{\mu} \, | u, m_u \rangle \right|^2 . \tag{12}$$

The summation on m_l, resp. m_u in the above expression extends over a complete basis of the state space associated to the level l, resp. u. Dipolar radiative transitions satisfy the following general selection rules:

$$p_u \neq p_l \tag{13}$$

$$\Delta J = 0, \pm 1 \tag{14}$$

$$J_l = 0 \not\leftrightarrow J_u = 0 \tag{15}$$

where p_u and p_l are the parities of levels u and l (the parity of a state designates its symmetry in a space reflexion), J_u and J_l are their associated total angular momentum quantum numbers, and $\Delta J = J_u - J_l$.

2.1.1 Atomic line spectra

A one-electron atomic state is defined by the quantum numbers n, l, m_l, s, m_s. n is the principal quantum number and takes positive integer value. l is the orbital angular momentum quantum

number and takes integer values between 0 and $n-1$. The numerical values of l can be replaced by letters $(s, p, d, f, g, h \ldots)$. The quantum numbers m_l and m_s are the projections of the orbital and spin momenta. The spin quantum number s is equal to $\frac{1}{2}$. For a many-electron atom, the wavefunction can be expressed in a first approximation in terms of product of one-electron atomic states nlm_l with the requirement of respecting the Pauli exclusion principle (impossibility to have 2 electrons in the same state, i.e. with the same quantum numbers). This allows to define a configuration by counting the number N of electrons in each subshell nl, using the notation nl^N. The ground state configuration for atomic nitrogen is denoted by $1s^2 2s^2 2p^3$, which indicates that two electrons are in the subshell $1s$, two are in the $2s$ one and three are in the $2p$ one. The two first excited state configurations of atomic nitrogen are $1s^2 2s^2 2p^2 3s$ and $1s^2 2s 2p^4$. In fact, we have to take into account the coupling of the different angular momenta of the incomplete subshell . Two extreme cases of coupling correspond to jj and LS coupling. The jj coupling occurs when the leading process is the coupling between orbital and spin angular momenta of an electron. In the LS coupling scheme, which corresponds to the atoms an ions considered here, the electron orbital angular momenta are coupled to give the total orbital angular momentum L, the electron spin angular momenta are coupled to give the total spin angular momentum S. The combination of a particular S value and particular L value gives a spectroscopic term ${}^{2S+1}L$ (the numerical values of $L = 0, 1, 2, \ldots$ are replaced by letters $S, P, D, \ldots$). The total angular momentum $\mathbf{J}$ is the sum of $\mathbf{L}$ and $\mathbf{S}$. The spin-orbit interaction splits the energy term ${}^{2S+1}L$ into $2 \times \min(L, S) + 1$ levels denoted ${}^{2S+1}L_J$ corresponding to the various total angular momentum values $J = |L - S|, |L - S| + 1, \ldots, L + S$ allowed for the term ${}^{2S+1}L$. Each energy level ${}^{2S+1}L_J$ has a $2J + 1$ degeneracy (without considering the nuclear spin).

The main radiative bound-bound transitions observed for atomic species are electric dipolar ones which satisfy the general selection rules given by Eqs. (13–15).

Moreover, if the upper and lower transition levels satisfy the pure LS coupling scheme, we have the additional selection rules for the electric dipolar transition

$$\Delta S = 0, \tag{16}$$

$$\Delta L = 0, \pm 1, \tag{17}$$

$$L = 0 \not\leftrightarrow L = 0 \tag{18}$$

where we have introduced the notations ΔS and ΔL concerning the total spin and total orbital angular momenta of the electrons in a similar way as for J.

Different spectroscopic databases are available which give for each transition $u \leftrightarrow l$ the transition frequency, the energy of the upper E_u or lower level E_l of the transition, the level degeneracies g_u and g_l, and the Einstein emission coefficient A_{ul} or the absorption oscillator strength, f_{lu} which is defined according to

$$f_{lu} = \frac{B_{lu} h \sigma_{ul}}{\pi r_e}, \tag{19}$$

$$= \frac{8\pi^2 m_e c}{3 h q_e^2} \sigma_{ul} \frac{1}{g_l} \sum_{m_l m_u} \left| \langle l, m_l | \boldsymbol{\mu} | u, m_u \rangle \right|^2, \tag{20}$$

where r_e, m_e and q_e are respectively the classical radius, the mass and the charge of the electron. Emission oscillator strengths are generally defined following the convention

$$f_{ul} = -\frac{g_l}{g_u} f_{lu}, \tag{21}$$

and even more symmetric oscillator strengths often are given in databases since we have the relation

$$g_l f_{lu} = -g_u f_{ul}. \tag{22}$$

To calculate the emission and absorption coefficient we need to know the populations n_u and n_l. At LTE the population of level i is given by

$$n_i = \frac{g_i N_a}{Q(T)} \exp\left(-\frac{E_i}{kT}\right), \tag{23}$$

where $Q(T)$ is the internal partition function of the radiating particle at temperature T, and N_a the total population of the radiating species. For a multi-temperature model, we use Eq. 23 at the temperature of electronic excitation.

For air plasma we have compared (cf Ref. [15]) three available databases: (i) the NIST database [16] which contains critical acclaimed data but is thus not a priori; (ii) the Hirata and Horaguchi [17] database which has been obtained by merging the 1989 updated Kurucz's [18] one, old NIST (1966,1988) ones, line positions from the Kelly database [19] and an earlier (1987) version of the TOPABSE data base (see next item); (iii) the TOPBASE database [20, 21] which is purely theoretical and does not include the fine structure. TOPBASE is an atomic database which concerns astrophysically abundant species (atomic number Z=1–26) and has been developed within the international Opacity Project since 1984 in order to estimate stellar envelope opacities. The database contains the most complete dataset of LS-coupling term energies, f-values and photoionization cross sections. They have been computed in the close-coupling approximation by means of the R-matrix method with innovative asymptotic techniques [22]. Two requisites were claimed: completeness and accuracy. For example, the database includes 1391 energy LS terms, and 18037 electric dipolar transitions concerning the neutral oxygen atom (OI).

Figure 1 shows a comparison between the numbers of lines included in the above cited databases for O, N species below 150000 cm^{-1}, and for O^+, N^+ species below 300000 cm^{-1}. Note that the Hirata database includes all lines from Kelly and Kurucz ones, so relevant comparisons concern HIRATA, NIST and TOPBASE databases. It must be again emphasized that the TOPBASE database does not include the fine structure, so the numbers of lines inlcuded in TOPBASE plotted in Fig. 1 are in fact numbers of multiplets. The optically thin emission of each atom or ion transition

$$\epsilon_{ul} = \frac{A_{ul}}{4\pi} hc\sigma_{ul} n_u \tag{24}$$

has been calculated from these three databases for an atmospheric LTE air plasma at 10000 K for N and O and at 20000 K for N^+ and O^+. Figure 2 gives an example for N and a temperature of 10000 K. Some misplaced multiplets in TOPBASE are observed in a few regions, which normally do not contribute to radiation. A few discrepancies exist between NIST and TOPBASE, with transitions lacking in NIST. The discrepancies are on the whole larger with Hirata base. The NIST database has been found to be complete enough to predict emission for the temperature range considered here. We have thus retained the NIST database for atom and ion line transitions.

Bound-bound atomic transitions may generally not be assumed to be optically thin in many applications (in particular for resonance transitions involving the ground energy term of the atom). We thus have to calculate the detailed high resolution absorption and emission spectra of the plasma for radiative transfer predictions. The spectral line shapes $f_{ul}(\sigma - \sigma_{ul})$ introduced in Eqs. (7-8) have thus to be determined. An extensive litterature has been devoted to the spectral line shapes of atomic species; some recent reviews may be found in Refs. [23, 24]. The main mechanisms which have to be accounted for in the case of atomic species are Doppler and collisional broadening: they may be treated independently with sufficient accuracy for the prediction of radiative transfer. The global line shape will thus be the convolution of line profile due to each mechanism.

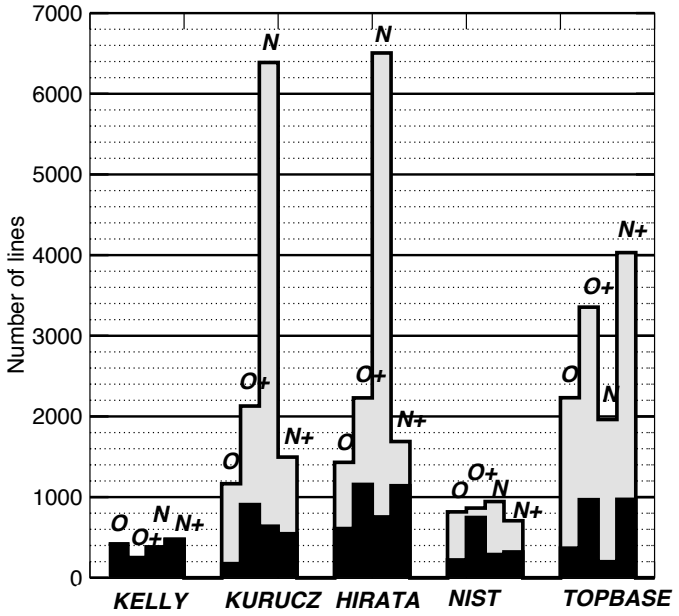

Figure 1: Number of O, O^+, N and N^+ lines included in the different atomic databases below 150000 cm^{-1} for atomic species and below 300000 cm^{-1} for ions. The numbers indicated in black correspond to atomic lines located above 28500 cm^{-1} (from Ref. [15]).

For the applications considered here, radiating particle velocities have a Maxwellian distribution, so the Doppler profile is a Gaussian

$$f_D(\sigma - \sigma_{ul}) = \sqrt{\frac{\ln 2}{\pi}} \frac{1}{\gamma_D} \exp\left[-\ln 2 \left(\frac{\sigma - \sigma_{ul}}{\gamma_D} \right)^2 \right] \tag{25}$$

whose half width at half maximum (HWHM) γ_D is expressed (in the same units as σ_{ul}) as:

$$\gamma_D = \sigma_{ul} \sqrt{\frac{2kT_r \ln 2}{m_r c^2}}. \tag{26}$$

In the above expression, T_r is the translation temperature of the radiator and m_r its mass.

Neutral collisional broadening is generally accounted for under the impact approximation (see Ref. [25]), leading to a Lorentzian profile of HWHM γ_{ul}^L

$$f_L(\sigma - \sigma_{ul}) = \frac{\gamma_{ul}^L}{\pi} \frac{1}{(\gamma_{ul}^L)^2 + (\sigma - \sigma_{ul})^2}. \tag{27}$$

γ_{ul}^L may be expressed as the sum of a van der Waals contribution $\gamma_{ul}^{\mathrm{vdw}}$ (corresponding to an interaction potential proportional to d^{-6}, d being the distance between particles) and of a resonance contribution $\gamma_{ul}^{\mathrm{res}}$ (potential proportional to d^{-3}) from the usual expressions given by Griem [25].

The van der Waals contribution is obtained from

$$\gamma_{ul}^{\mathrm{vdw}} = \frac{1}{2c} \sum_p N_p \left\langle v^{\frac{3}{5}} \right\rangle \left(\frac{9\pi\hbar^5 |\Delta\overline{r^2}|}{16 m_e^3 E_p^2} \right)^{\frac{2}{5}}, \tag{28}$$

where N_p is the population of the neutral perturber p, E_p the energy of the first perturber excited state which mainly determines its polarizability. $\Delta\overline{r^2} = \overline{r_u^2} - \overline{r_l^2}$ is the difference between

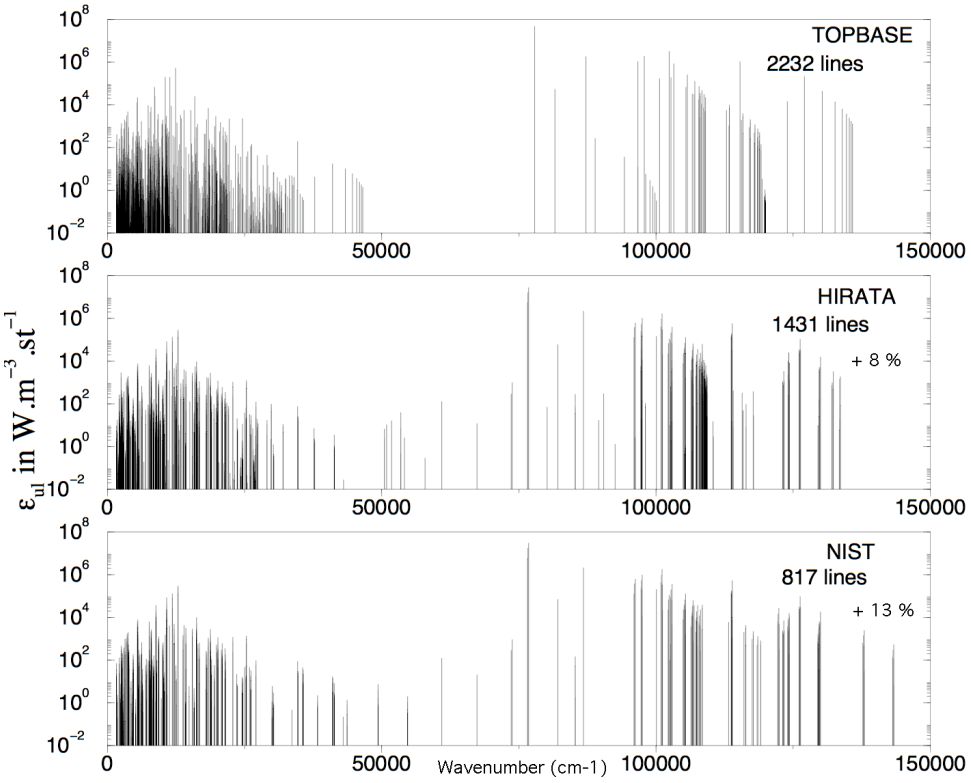

Figure 2: Comparison between the emissivities of O lines included in TOPBASE, HIRATA and NIST databases at 10000 K (from Ref. [15]).

the mean square radii of the radiating particle in the upper and lower transition levels if the perturber and the radiator are particles of different type; for identical particles, only the term $\overline{r^2}$ associated to the level u or l of the same parity as the radiator ground level is included in the above difference — the other level will contribute to the resonance broadening (see below). The symbol $\langle\cdot\rangle$ designates an average according to the distribution of the relative velocity v of the perturber. For a Maxwellian distribution at temperature T_p, this average is expressed as

$$\left\langle v^{\frac{3}{5}} \right\rangle = \frac{\Gamma(\frac{18}{5})}{2^{\frac{8}{5}}\Gamma(\frac{23}{10})} \left(\frac{2kT_p}{m_p}\right)^{\frac{3}{10}}, \tag{29}$$

where m_p is the reduced mass of the radiator-perturber couple.

The resonance contribution occurs only for perturbers of the same type as the radiator and is expressed according to

$$\gamma_{ul}^{\text{res}} = \frac{3q_e^2}{16\pi^2\epsilon_0 m_e c^2} \sum_j n_j \left(\sqrt{\frac{g_j}{g_u}} \left| \frac{f_{ju}}{\sigma_{uj}} \right| + \sqrt{\frac{g_j}{g_l}} \left| \frac{f_{jl}}{\sigma_{lj}} \right| \right), \tag{30}$$

where the summation extends over the levels j of the radiator; note that for a given j level in this summation, only one of the two terms does not vanish since u and l parities differ.

Last, broadening due to collisions with charged particles (electron and ions), known as Stark broadening has to be accounted for. For entry plasmas which are usually at quite medium pressure and weakly ionized, and for non hydrogenoid species considered here, the impact approximation may be used for electron and ion contributions. One may use simple expressions

obtained from semi-clasical adiabatic approach [26] which are similar to those given above for neutral contribution. As an example, for a neutral radiator, the Stark line width (HWHM) will be expressed as the sum of a dipolar contribution

$$\gamma_{ul}^{\mathrm{dip}} = N_p \frac{1}{2\pi c} \left(\frac{\pi}{2}\right)^{5/3} \Gamma\left(\frac{1}{3}\right) |\Delta C_4|^{2/3} \left\langle v^{\frac{1}{3}} \right\rangle, \tag{31}$$

and a quadupolar one

$$\gamma_{ul}^{\mathrm{quad}} = N_p \frac{\pi}{2c} \Delta C_3, \tag{32}$$

where the ΔC_4 and ΔC_3 parameters characterize resp. the dipolar polarization interaction potential (proportional to d^{-4}) and quadrupolar one (proportional to d^{-3}) and may be expreesed according to [26]

$$\Delta C_4 = C_{4u} - C_{4l}, \tag{33}$$

$$C_{4j} = \frac{I_H^2}{\pi m_e h c^2} \left(\frac{a_0 q_p}{q_e}\right)^2 \sum_{\ell} \frac{f_{j\ell}}{\sigma_{j\ell}^2}, \tag{34}$$

$$\Delta C_3 = \sqrt{\left(B_u \overline{r_u^2}\right)^2 + \left(B_l \overline{r_l^2}\right)^2 - B_{ul} \overline{r_u^2 r_l^2}} \sqrt{\frac{2I_H}{m_e}} \left|\frac{q_p}{q_e}\right|. \tag{35}$$

In the above expressions, I_H is the Rydberg constant, a_0 the Bohr radius and q_p the perturber charge. B_j and B_{ul} constants may be crudely estimated from the total electronic angular momentum quantum numbers L_u and L_l of the radiator according to

$$B_j = \sqrt{\frac{2L_j+1}{15}} \begin{pmatrix} L_j & 2 & L_j \\ 0 & 0 & 0 \end{pmatrix} (-)^{L_j}, \tag{36}$$

$$B_{ul} = -2 B_u B_l \begin{Bmatrix} L_u & L_l & 1 \\ L_l & L_u & 2 \end{Bmatrix}. \tag{37}$$

Similar expressions concerning ionized radiators may be found in Ref. [27].
More sophisticated semi-classical approaches [27, 28, 29, 30], beyond the previous adiabatic approach, have been used for the present database. They enable to achieve better accuracy even if their use remains quite tedious in the framework of radiative transfer applications where systematic calculations are required.

2.1.2 Diatomic line spectra

The total hamiltonian H_{tot} of an isolated diatomic molecule can be written, without taking into account the hyperfine structure due to nuclear spin of nuclei [31], as:

$$H_{tot} = -\sum_{\alpha=1}^{2} \frac{h^2}{8\pi^2 M_\alpha} \nabla_\alpha^2 - \sum_{i=1}^{N_e} \frac{h^2}{8\pi^2 m_e} \nabla_i^2 + V_{n,n} + V_{n,e} + V_{e,e} + H_{sf} \tag{38}$$

were M_α is the mass of nucleus α and m_e the electron mass. The first two terms correspond to the nuclear and electronic kinetic energy. The following terms correspond to the nuclear-nuclear potential energy, the nuclear-electron potential energy, the electron-electron potential energy. The last term H_{sf} includes the different terms linked to interaction of spin and angular momenta leading to the fine structure:

$$H_{sf} = H_{SO} + H_{SS} + H_{SR} \tag{39}$$

$H_{SO} = A(r)\mathbf{L}.\mathbf{S}$ is the so-called spin orbit interaction which represents the interaction of the electron spin characterized by spin angular momentum $\mathbf{S}$ with the magnetic field created by electron motion characterized by the orbital angular momentum $\mathbf{L}$. $H_{SS} = \epsilon(r)[3S_z^2 - S^2]$ is the so-called spin-spin interaction, S_z being the projection of $\mathbf{S}$ on the internuclear axis. $H_{SR} = \gamma(r)\mathbf{N}.\mathbf{S}$ is the so-called spin-rotation interaction where $\mathbf{N}$ is the sum of the orbital electronic angular momentum $\mathbf{L}$ and the rotational angular momentum $\mathbf{R}$ ($\mathbf{N}$=$\mathbf{L}$+$\mathbf{R}$).
The level energies and wavefunctions which are required to calculate line positions (Eq. 6) and transition probabilities (Eq. 12) correspond to the eigenvalues and eigenfunctions of the total hamiltonian.

Characterization of a rotational state
The Born-Oppenheimer approximation which separates the electronic and nuclear motions allows to define electronic states. Similarly to atoms there is a coupling between electronic spin and orbital angular momenta. For molecules with light nuclei, this coupling is weak and we can define the projection of the total electronic orbital momentum $\mathbf{L}$ on the intermolecular axis. The absolute value of this projection is noted Λ. An electronic state of a diatomic molecule is characterized by the label $^{2S+1}\Lambda$ where $2S+1$ is the spin multiplicity. The numerical values 0,1,2,... of Λ are replaced by Σ, Π, Δ, ... To differentiate states with the same S and Λ values, a letter is added which is generally X for the ground state, then A,B,C,... for a spin multiplicity, a,b,c,... for another spin multiplicity, etc .... Additional labels, g or u, can be added to characterize for homonuclear molecules the symmetry of the electronic wave function with respect to the inversion operation $\hat{i}$ in the molecular frame, and + or − to characterize for Σ states the symmetry of the electronic wavefunction with respect to the symmetry operator $\hat{\sigma_v}$ which corresponds to a reflexion through a plane containing the internuclear axis.
For $\Lambda > 0$ there is a double orbital degeneracy called Λ- doubling which will be lifted in the rotating molecule. The electronic degeneracy is thus equal to $(2 - \delta_{0,\Lambda})(2S + 1)$.

If we consider the rotating and vibrating molecule, a rotational level (or rovibronic level) will be characterized by the five quantities n, v, J, i, p which correspond to:
n: the electronic state
v: the vibrational number
J: the total angular momentum without nuclear spin ($\mathbf{J}$= $\mathbf{L}$ + $\mathbf{S}$ + $\mathbf{R}$)
i: the spin multiplet component which takes 2S+1 values
p: the parity which characterizes the symmetry of the total wavefunction (without nuclear spin) with respect to the symmetry operator I. The parity takes (2-$\delta_{0,\Lambda}$) values.

The multiplet structure will depend on how the electronic angular momenta couple to the molecular rotation. Several limiting coupling cases are defined: the Hund's coupling case a, b, c, d, ... We are, in the present study, concerned by the cases a and b. In Hund's case a, the interaction between the molecular rotation and the electrons motion is weak, $\mathbf{L}$ and $\mathbf{S}$ are closely coupled to the internuclear axis, their projections being Λ and Σ. Since $\mathbf{R}$ is at right angle to the internuclear axis, the projection of $\mathbf{J}$ on the internuclear axis, Ω, corresponds to $\Omega = \Lambda + \Sigma$. The quantum number J takes the values $|\Omega|$+1, $|\Omega|$+2, ... In Hund's case b, $\mathbf{S}$ does not couple to the internuclear axis and recouples to $\mathbf{N}$ = $\mathbf{L}$+$\mathbf{R}$. J can have all integer values from N+S to N-S. An intermediate a/b coupling has been considered for most of the states considered here.

Energy of a rotational state
The energy of the rotational level (n, v, J, i, p) can be expressed as the sum of an electronic

contribution, a vibrational contribution and a rotational contribution:

$$E^n_{v,i}(J,p) = E_{el}(n) + E_{vib}(n,v) + E_{rot}(n,v,J,i,p) \tag{40}$$

A very crude approximation consists in considering that the molecule vibrates like an harmonic oscillator, rotates like a rigid rotor and to neglect the fine structure. In this case we obtain a very simple expression for the energy:

$$E^n_{v,i}(J,p) = E_{el}(n) + \hbar\omega(v+1/2) + BJ(J+1) \tag{41}$$

where $\hbar\omega$ is the vibration frequency and B is the rotation constant.

We have used experimentally determined energies or more precisely experimentally determined parameters which allow to recalculate the energies. Theoretically [32, 33], the complete hamiltonian is expressed on a basis set of rotational-vibration-electronic wavefunctions which correspond to Hund's case a. A series of contact transformations is performed to remove or weaken off-diagonal matrix elements. The final effective or model hamiltonian leads to energy expressions which involve a limited number of parameters which are fitted to experimental data. We give two examples of such developments, one for a simple case, the singlet state $^1\Sigma$, and one for a more difficult case, the doublet state $^2\Pi_u$. The expressions used for the other types of states can be found in [15, 11].
The level energies for $^1\Sigma$ state are given by:

$$E^{1\Sigma}_v(J) = T_v + B_v x - D_v x^2 + H_v x^3 \tag{42}$$

with $x = J(J+1)$.
The reduced matrix for the $^2\Pi_u$ state and for given v, J, and parity has two dimensions:

$$M = \begin{vmatrix} T_\Lambda & H_\Lambda \\ H_\Lambda & T_1 \end{vmatrix}$$

with [34]:

$$\begin{aligned} T_{v,\Lambda}(J) &= T_v - \frac{A_v}{2} + (B_v - A_{Dv})x^2 - D_v\left[x^4 + x^2 - 1\right] + \\ &\quad \frac{1 \pm x}{2}\left[p_v + q_v\left(1 \pm x\right)\right] + H_v x^2\left[x^4 + 6x^2 - 7\right] \qquad (43) \\ T_{v,1}(J) &= T_v + \frac{A_v}{2} + (B_v + A_{Dv})\left[x^2 - 2\right] - D_v\left[\left(x^2-2\right)^2 + x^2 - 1\right] + \\ &\quad \frac{q_v}{2}\left[x^2 - 1\right] + H_v x^2\left[x^4 + 7\right] \qquad (44) \\ H_{v,\Lambda}(J) &= 2D_v\left[x^2-1\right]^{\frac{3}{2}} - \left[B_v + \frac{p_v}{2} + \frac{q_v}{2}\left(1 \pm x\right)\right]\left[x^2-1\right]^{\frac{1}{2}} + \\ &\quad H_v\left[x^2-1\right]^{\frac{1}{2}}\left[x^2\left(3x^2+1\right)\right] \qquad (45) \end{aligned}$$

where $x = J + \frac{1}{2}$. The Λ-doubling is accounted for through the $\pm$ values in these expressions.

The diagonalization of this matrix leads to the following expressions for the energies for the two multiplet components:

$$\begin{aligned} E^{^2\Pi}_{v,1} &= \frac{1}{2}\left[T_{v,1}(J) + T_{v,\Lambda}(J) - \left((T_{v,1}(J) - T_{v,\Lambda}(J))^2 + 4H^2_{v,\Lambda}(J)\right)^{\frac{1}{2}}\right] \qquad (46) \\ E^{^2\Pi}_{v,2} &= \frac{1}{2}\left[T_{v,1}(J) + T_{v,\Lambda}(J) + \left((T_{v,1}(J) - T_{v,\Lambda}(J))^2 + 4H^2_{v,\Lambda}(J)\right)^{\frac{1}{2}}\right] \qquad (47) \end{aligned}$$

Radiative transitions

A rotational line will correspond to the transition between two rotational states characterized by (n', v', J', i', p') and $(n'', v'', J'', i'', p'')$ such that the matrix element of the electric dipole moment operator (Eq. 12) does not vanish. Such transitions obey to the general selection rules given by Eqs. (13–15) and to additional selection rules for Hund's cases a and b:

$$\Delta\Lambda = 0, \pm 1, \tag{48}$$

$$\Delta S = 0. \tag{49}$$

The set of transitions between rovibrational levels of the electronic states A and B will be called the A-B system. The transitions between the vibrational level v' of A and the vibrational level v" of B will be called the v'-v" vibrational band. Finally transitions between A,v' and B,v" with the same ΔN and ΔJ are called branchs and are represented by:

$$^{Y}X_{ij} \tag{50}$$

where i and j designate the substates of the spin-multiplet of the upper level and of the lower level. X and Y correspond to the change in J and N and are denoted by the symbols given in Fig. 3. The different branchs corresponding to a $^2\Pi_r - ^2\Pi_r$ system are shown schematically in Fig. 4.

	T	S	R	Q	P	O	N
$\Delta J = J' - J''$			1	0	-1		
$\Delta N = N' - N''$	3	2	1	0	-1	-2	-3

Figure 3: Notation of the different branches according ΔJ and ΔN values.

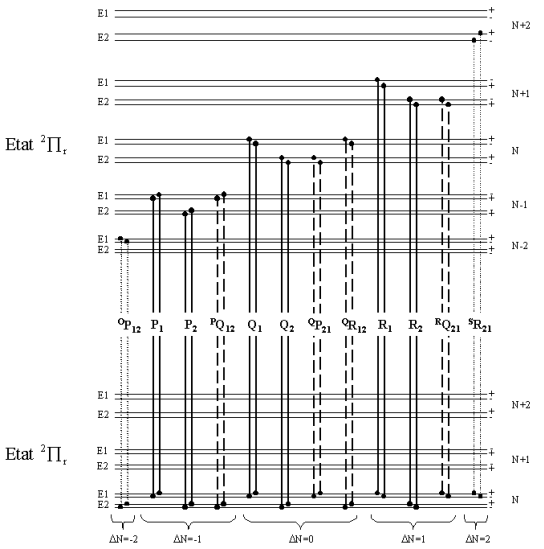

Figure 4: Branch strucure for a $^2\Pi_r - ^2\Pi_r$ system when the two states are close to Hund's case b; N is even in this example (from [9]).

The strength of the different transitions will depend on the transition probability R_{ul} defined in Eq. 12 which is written as the product of two terms

$$R_{ul} = (R_e^{v'v''})^2 S_{J'J''}^{v'v''}. \tag{51}$$

$(R_e^{v'v''})^2$ is the square of the electronic vibrational transition moment, and $S_{J'J''}^{v'v''}$ is the Hönl-London factor. These quantities are defined following the convention of Whiting et al. [35] which results in the uniform sum rule for the Hönl-London factors:

$$\sum_{J'} S_{J'J''}^{v'v''} = (2 - \delta_{0,\Lambda'}\delta_{0,\Lambda''})(2S+1)(2J''+1) \tag{52}$$

The electronic-vibrational part of line intensity is given by:

$$\left(R_e^{v'v''}\right)^2 = \left[\int_0^\infty \psi_{v'}(r) R_e(r) \psi_{v''}(r) dr\right]^2, \tag{53}$$

where r is the internuclear distance, $\psi_{v'}(r)$ and $\psi_{v''}(r)$ are the radial rotationless vibrational wavefunctions in the vibrational levels v' (of the upper electronic state of the transition) and v'' (of the lower electronic state) respectively. $R_e(r)$ is the electronic transition moment function (ETMF).

We need to know $\left(R_e^{v'v''}\right)^2$ for all the contributing bands. This information can be extracted from spectroscopic measurements but is far to be complete. To remedy this lack of experimental data, the electronic-vibrational part of line intensities have been calculated systematically. The method comprises three steps.

In a first step, the potential curves for all the elecronic states have been reconstructed via the Rydberg-Klein-Rees (RKR) procedure [36, 37, 38] which allows to calculate the classical turning points $r_{inner}(v)$, $r_{outer}(v)$ from the vibrational term energy $G(v)$ and rotational spectroscopic constant B_v through the equations:

$$r_{inner}(v) = \sqrt{\frac{f(v)}{g(v)} + f(v)^2} - f(v), \tag{54}$$

$$r_{outer}(v) = \sqrt{\frac{f(v)}{g(v)} + f(v)^2} + f(v), \tag{55}$$

where:

$$f(v) = \frac{h}{2\pi\sqrt{2\mu_r}} \int_{v_0}^{v} \frac{1}{\sqrt{G(v) - G(v')}} dv', \tag{56}$$

$$g(v) = \frac{2\pi\sqrt{2\mu_r}}{h} \int_{v_0}^{v} \frac{B_{v'}}{\sqrt{G(v) - G(v')}} dv'. \tag{57}$$

In Eqs. (56,57), μ_r is the reduced mass of the molecule, v_0 is the zero of $G(v)$, $G(v)$ and B_v are Dunham expansions in $(v + \frac{1}{2})$:

$$G(v) = \sum_{i=0}^{n} Y_{i0} \left(v + \frac{1}{2}\right)^i, \tag{58}$$

$$B_v = \sum_{i=0}^{m} Y_{i1} \left(v + \frac{1}{2}\right)^i. \tag{59}$$

The resulting potential curve $U_{RKR}(r)$ was extrapolated by using a repulsive function $U_{inner}(r)$ (inner turning points) and a Hulburt and Hirschfelder potential [39] $U_{outer}(r)$ (outer turning points):

$$U_{inner}(r) = \frac{a_1}{r^{b_1}}, \tag{60}$$

$$U_{outer}(r) = D_e \left[1 - e^{-a_2(r-r_e)}\right]^2 + D_e \left[b_2 a_2^3 (r - r_e)^3 e^{-2a_2(r-r_e)} \left(1 + a_2 c_2 (r - r_e)\right)\right], \tag{61}$$

where D_e is the dissociation energy of the electronic state considered relative to the bottom of the potential energy curve, and r_e is the equilibrium internuclear distance. a_1, b_1 and a_2, b_2, c_2 and r_e are the floating parameters adjusted in order that each extrapolation function fits a significant part of each extremity of the RKR potential $U_{RKR}(r)$.

In a second step, the resulting potential $U_{final}(r)$ is used in the radial Schrödinger equation to solve for the rotationless-vibrational wavefunctions $\psi_v(r)$ using a Chebyshev expansion method. We checked that the difference between reconstructed and initial energies remains small (lower than 0.14% on the maximal v_{max}).

Finally, $\left(R_e^{v'v''}\right)^2$ is evaluated by using electronic transition moment function $R_e(r)$ selected in the litterature [9, 12]. Figure 3 shows an illustration of the above described procedure in the

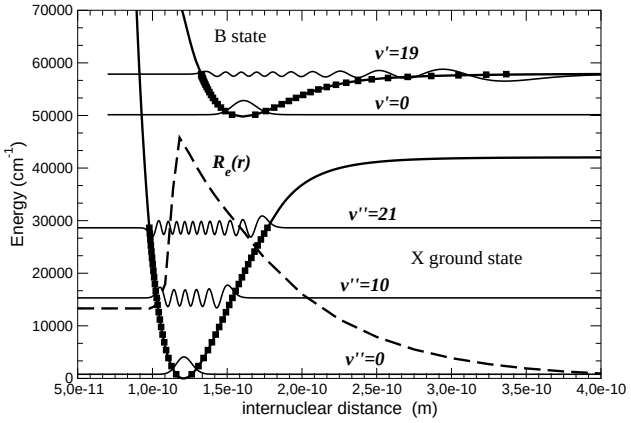

Figure 5: Reconstructed potentials for the O_2 Schumann-Runge (B-X) system. The RKR reconstructed potentials are represented by points. A few vibrational functions are represented with the selected transition moment function (adapted from [9]).

case of the O_2 Schumann-Runge $B^3\Sigma_u^- - X^3\Sigma_g^-$ transition.

Diatomic database

We have calculated an exhaustive spectroscopic database including the main electronic systems of the diatomic molecules N_2, N_2^+, O_2, NO, CO, C_2, CN, CO^+ which contribute to radiative transfer in N_2 – O_2 – CO_2 plasmas. These systems are listed in Table 2. For each of these 35 systems, potential curves have been calculated according to the above described procedure from up-to-date deperturbed — when available — Dunham coefficients. Electronic transition moments have been critically selected in the literature and squared electronic vibrational transition moments have been systematically obtained for the bands listed in Table 2. Systematic validations have been achieved by comparing experimental or theoretical vibrational radiative life times available in the literature to those calculated from our vibrational transition moments. Rotational line positions and strengths have thus been calculated from up-to-date carefully selected spectroscopic constants. Fine structure has been introduced considering the intermediate Hund's case between a and b cases ($\Sigma - \Sigma$ transitions have been calculated considering the pure Hund's case b). Λ-doubling has been accounted for when data were available. Hönl-London factors of Ref. [40] have been used. Regarding perturbations, rotational perturbations which

Table 2: Calculated diatomic electronic systems

molecule	system name	upper state – lower state	Calculated bands $(0:v'_{max}, 0:v''_{max})$
N_2	First-Positive	$B^3\Pi_g$–$A^3\Sigma_u^+$	$(0:21;0:16)$
	Second-Positive	$C^3\Pi_u$–$B^3\Pi_g$	$(0:4;0:21)$
	Birge-Hopfield 1	$b^1\Pi_u$–$X^1\Sigma_g^+$	$(0:19;0:15)$
	Birge-Hopfield 2	$b'^1\Sigma_u^+$–$X^1\Sigma_g^+$	$(0:28;0:15)$
	Carroll-Yoshino	$c'_4{}^1\Sigma_u^+$–$X^1\Sigma_g^+$	$(0:8;0:15)$
	Worley-Jenkins	$c_3{}^1\Pi_u$–$X^1\Sigma_g^+$	$(0:4;0:15)$
	Worley	$o_3{}^1\Pi_u$–$X^1\Sigma_g^+$	$(0:4;0:15)$
N_2^+	Meinel	$A^2\Pi_u$–$X^2\Sigma_g^+$	$(0:27;0:21)$
	First-Negative	$B^2\Sigma_u^+$–$X^2\Sigma_g^+$	$(0:8;0:21)$
	Second-Negative	$C^2\Sigma_u^+$–$X^2\Sigma_g^+$	$(0:6;0:21)$
NO	γ	$A^2\Sigma^+$–$X^2\Pi_r$	$(0:8;0:22)$
	β	$B^2\Pi_r$–$X^2\Pi_r$	$(0:37;0:22)$
	δ	$C^2\Pi_r$–$X^2\Pi_r$	$(0:9;0:22)$
	ϵ	$D^2\Sigma^+$–$X^2\Pi_r$	$(0:5;0:22)$
	γ'	$E^2\Sigma^+$–$X^2\Pi_r$	$(0:4;0:22)$
	β'	$B'^2\Delta$–$X^2\Pi_r$	$(0:6;0:22)$
	11000 Å	$D^2\Sigma^+$–$A^2\Sigma^+$	$(0:5;0:8)$
	infrared	$X^2\Pi_r$–$X^2\Pi_r$	$(0:22;0:22)$
O_2	Schumann-Runge	$B^3\Sigma_u^-$–$X^3\Sigma_g^-$	$(0:19;0:21)$
CO	Infrared	$X^1\Sigma^+ - X^1\Sigma^+$	(0:50;0:50)
	Fourth Positive	$A^1\Pi - X^1\Sigma^+$	(0:23;0:50)
	Hopfield-Birge	$B^1\Sigma^+ - X^1\Sigma^+$	(0:2;0:50)
	Third Positive	$b^3\Sigma^+ - a^3\Pi$	(0:2;0:18)
CO^+	Comet-tail	$A^2\Pi_i - X^2\Sigma^+$	(0:33;0:31)
	Baldet-Johnson	$B^2\Sigma^+ - A^2\Pi_i$	(0:33;0:50)
	First Negative	$B^2\Sigma^+ - X^2\Sigma^+$	(0:22;0:35)
CN	Red	$A^2\Pi_i - X^2\Sigma^+$	(0:38;0:34)
	Violet	$B^2\Sigma^+ - X^2\Sigma^+$	(0:25;0:36)
	LeBlanc	$B^2\Sigma^+ - A^2\Pi_i$	(0:25;0:38)
C_2	Philips	$A^1\Pi_u - X^1\Sigma_g^+$	(0:35;0:21)
	Mulliken	$D^1\Sigma_u^+ - X^1\Sigma_g^+$	(0:22;0:21)
	Deslandres-D'Azambuja	$C^1\Pi_g - A^1\Pi_u$	(0:9;0:32)
	Ballik et Ramsay	$b^3\Sigma_g^- - a^3\Pi_u$	(0:41;0:39)
	Swan	$d^3\Pi_g - a^3\Pi_u$	(0:18;0:33)
	Fox-Herzberg	$e^3\Pi_g - a^3\Pi_u$	(0:15;0:35)

affect a few J values of a given vibrational level have not been modelled. For strong homogeneous perturbations such as those encountered for the five N_2 $b'^1\Sigma_u^+$, $c_4'^1\Sigma_u^+$, $b^1\Pi_u$, $c_3{}^1\Pi_u$, and $o_3{}^1\Pi_u$ excited states, and for the two NO $B^2\Pi_r$ and $C^2\Pi_r$ excited states, perturbed molecular constants have been used.

Rotational lines have been calculated up to the last rotational quantum number below the centrifugal dissociation of the upper and lower vibrational levels, i.e. widely beyond the validity range of the selected spectroscopic constants. Such extrapolations are required insofar as this database is devoted to predict radiative transfer inside very high rotational temperature plasmas. We have ensured that no aberrant line positions occur due to these extrapolations.

References from which the various selected spectroscopic constants and electronic transition moments have been taken are given in Ref. [9] for N, O plasma molecules and from Ref. [12] for carbonaceous molecules. Detailed systematic validations for each system may also be found in these two references.

For each of these lines, a Voigt line profile, taking into account Doppler, collisional and, when required, predissociative broadening has been adopted. For IR rovibrational transitions, detailed descriptions of collisionnal broadening parameters are available in Refs. [41, 42] for NO and in Ref. [43] for CO IR systems. However, data concerning collisional broadening of diatomic rovibronic lines remain quite scarce. We have used for all NO UV lines the collisional HWHM from Ref. [44]

$$\gamma_c^{NO_{UV}} = 0.293 \left(\frac{295}{T}\right)^{0.75} \text{cm}^{-1}\text{atm}^{-1}, \tag{62}$$

where T is the translational temperature of the heavy particles. For all other systems, we have used the pragmatic collisional line width

$$\gamma_c = 0.1 \left(\frac{273}{T}\right)^{0.7}, \tag{63}$$

following the values obtained in Ref. [45]. Finally, we have introduced predissociative (lorentzian) line widths form Refs. [46, 47, 48, 49, 50, 51], [52], and [53] for the N_2 VUV, NO, and O_2 systems, respectively.

The database enables to calculate any absorption or emission spectra for the considered electronic systems from the populations of molecular energy levels according to Eqs. 7-8. For media at LTE, the populations are caculated in a straightforward manner from the Boltzmann distribution and from the chemical composition. For nonequilibrium media, a currently used approximation is the two-temperature model, T_{rot} for the translational motion of heavy particles and rotation of molecules, T_{ve} for molecular vibration, electronic excitation, and free electron translation. In the framework of this two-temperature model, the population of an energy level (n, v, J, i, p) is expressed as

$$n_{nvJip} = n_r g_{s_{nJip}} \frac{2J+1}{Q(T_{ve}, T_{rot})} \exp\left(-\frac{E_{el}(n) + E_{vib}(n,v)}{kT_{ve}} - \frac{E_{rot}(n,v,J,i,p)}{kT_{rot}}\right) \tag{64}$$

where $Q(T_{ve}, T_{rot})$ is the two-temperature partition function [54], n_r is the total population of the considered molecule. The factor $g_{s_{nJip}}$ is the nuclear spin statistical factor which applies only for homonuclear molecules.

2.1.3 CO_2 spectra

Infrared contribution

It is well known that CO_2 is very active in the infrared. In its fundamental electronic state,

$X^1\Sigma_g^+$, the molecule is linear and possesses three modes of vibration: a symmetric stretching mode ν_1, a bending mode ν_2 (doubly degenerated) and an asymmetric stretching mode ν_3. The three modes are close to 1351, 672 and 2396 cm^{-1}. The modelling of CO_2 radiative properties at high temperature is a challenging problem due to the different couplings which have to be correctly described: Fermi resonance between symmetric and bending modes which gathers the levels in polyads, Coriolis effect which couples bending and antisymmetric modes, ...

The spectroscopy of CO_2 in the infrared has been the subject of a lot of experimental studies. The HITRAN [55] molecular spectroscopic database compiles the up-to-date spectroscopic data for this molecule and 38 other molecules. It is regularly improved. However this database has been primarily developed for low temperature applications and is not complete at high temperature; it does not include the transitions from high-excited rovibration states.
A few attempts have been made to generate data suitable for use at high temperature especially for gases involved in combustion and in particular for CO_2. The HITEMP [56] database has been calculated using a direct diagonalization method and is adapted to temperatures up to 1000 K. A similar technique but with a better treatment of the Coriolis operator has been used to generate a basis for applications up to 2000 K [57]. An approach based on effective operators has been used by Tashkun et al to generate the CDSD-1000 database [58] which is able to reproduce successfully the high-resolution spectra at low and medium temperatures and satisfactorily the medium resolution spectra at temperatures up to 3000K. We use the HITELOR database [59]. This database enlarges the HITRAN data by using approximate and empirical formulas for vibrational band intensities and by computing energies through a diagonalization of the Fermi matrix associated to the different polyads. The HITELOR databank has been succesfully used to simulate medium-resolution spectra at temperatures up to 2850 K. The database covers the 2.7, 4.4 and 15 μm regions which are the most important in terms of radiative transfer. All the transitions associated to a lower vibrational level lower than 13000 cm^{-1} have been accounted for. The maximal rotational number J is 200.
The pressure-broadening parameters and their temperature dependance have been calculated semiclassically up to J=101 [60]. For $J > 101$, the broadening coefficients have been set to their J=101's values.

Figures 6, 7, 8 and 9 show the calculated absorption coefficients for a CO(50%)-CO2(50%) mixture at 3600 K and a pressure of 100 Pa. These values are typical of those encountered in a Mars entry (see Sec. 3).

VUV, UV and visible contributions

As could be expected the electronic spectra of CO_2 is rather complicated. Two phenomena have been retained: the UV and VUV absorption and the chemiluminescence.They have been observed in shock tubes and flames and could have a potentially significant contribution in the considered applications.
The absorption cross sections of CO_2 at room temperature are available in the spectral range 50000 – 83000 cm^{-1} [61, 62]. They have also been measured in shock tubes between 28600 and 52000 cm^{-1} up to 3050 K [63, 64]. In this spectral region, the absorption is spectrally smooth and is mainly attributed to predissociative transitions in the $X^1\Sigma_g^+ \rightarrow^1 B_2$ system. The contribution of this mechanism has been estimated by using the analytical expression of the cross section $\sigma(\lambda, T)$ proposed in Ref. [64] :

$$\sigma(\lambda, T) = \frac{\sigma_{eff}}{Q_{vib}} \exp(-\epsilon_1(\lambda)/kT) \tag{65}$$

where Q_{vib} is the vibrational partion function of CO_2 and $\epsilon_1(\lambda)$ corresponds to an effective absorbing level.

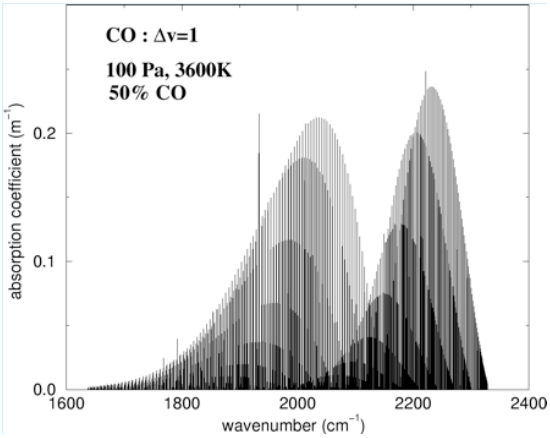

Figure 6: Absorption coefficient for the Δv=1 bands of CO.

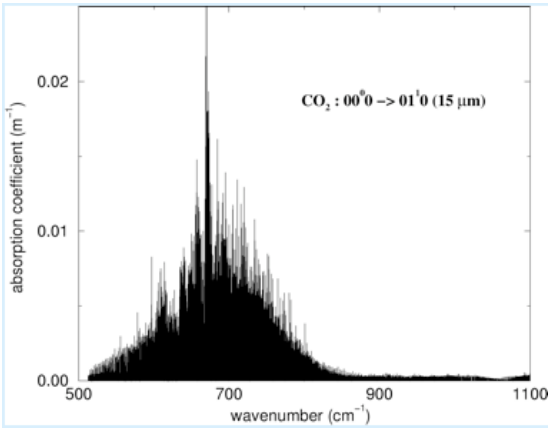

Figure 7: CO_2 absorption coefficient in the 15 μm region

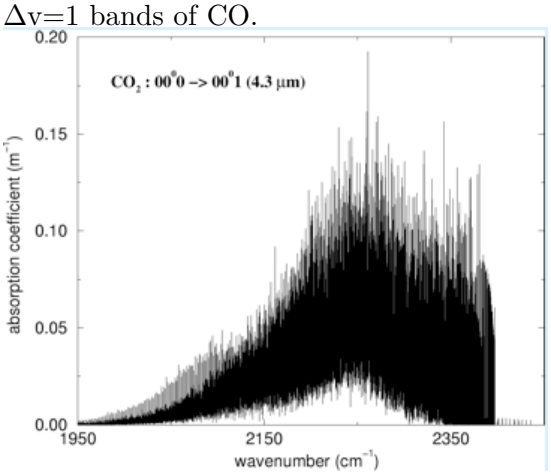

Figure 8: CO_2 absorption coefficient in the 4.3 μm region

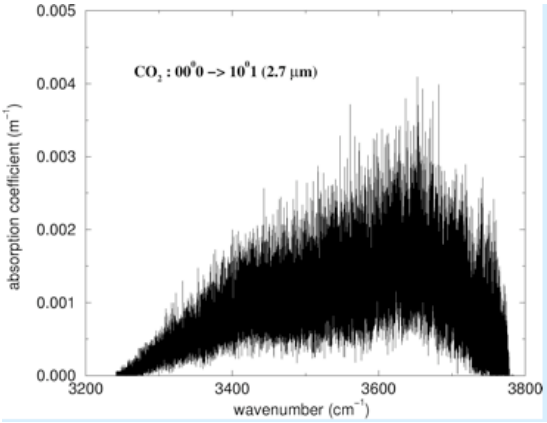

Figure 9: CO_2 absorption coefficient in the 2.7 μm region

The chemiluminescence resulting from the radiative combination of carbon monoxide and atomic oxygen,

$$CO + O \rightarrow CO_2 + hc\sigma, \tag{66}$$

is also believed to involve the electronic transition $^1B_2 -> X^1\Sigma_g^+$. The emission coefficient may be expressed as:

$$\eta_\sigma = N_O N_{CO} A_\sigma \exp(b_\sigma / T) \tag{67}$$

where N_O and N_{CO} are the populations of O and CO. The parameters A_σ and b_σ have been adjusted on the shock tube data of Slack and Grillo [65, 66] in the spectral range 15000 - 40000 cm^{-1} and for temperatures ranging from 1300 to 3000 K [11].

2.2 Bound-free transitions

Bound-free transitions correspond to photonization, photodissociation and photodetachment. They can be represented formally by:

$$AB(k) + hc\sigma \rightarrow A(i) + B(j) \tag{68}$$

The energy conservation leads to:

$$hc\sigma = \frac{1}{2}\mu g^2 + E_i^A + E_j^B - E_k^{AB}, \tag{69}$$

where μ is the reduced mass of the the products (A,B), g is the relative velocity of the products, E_l^X is the energy of level l of species X. The emission coefficient, the induced emission coefficient and the true absorption coefficient can be expressed as a function of the level-to-level cross sections relative to the spontaneous emission, $S_{ij,k}^{es}(\sigma)$, to the induced emission, $S_{ij,k}^{ei}(\sigma)$, and to the absorption, $S_{k,ij}^{abs}(\sigma)$, by:

$$\eta_{\sigma,fb} = \sum_{ijk} n_i^A n_j^B \, hc\sigma \, g S_{ij,k}^{es}(\sigma) 4\pi g^2 f^0(g) \frac{\mathrm{d}g}{\mathrm{d}\sigma} \tag{70}$$

$$\kappa_{\sigma,fb}^{ei} = \sum_{ijk} n_i^A n_j^B \, hc\sigma \, g S_{ij,k}^{ei}(\sigma) 4\pi g^2 f^0(g) \frac{\mathrm{d}g}{\mathrm{d}\sigma} \frac{1}{c} \tag{71}$$

$$\kappa_{\sigma,fb}^{abs} = \sum_{ijk} n_k^{AB} \, hc\sigma \, S_{k,ij}^{abs}(\sigma) \frac{1}{c} \tag{72}$$

where n_l^X designates the population of the level l of species X, and $f^0(g)$ is the distribution function of the relative velocities of the dissociation products.
By considering that at equilibrium the radiation intensity must follow the Planck's law, we can write relations similar to the Einstein-Milne ones [67] between the three level-to-level cross sections:

$$\frac{S_{ij,k}^{es}(\sigma)}{S_{ij,k}^{ei}(\sigma} = 2hc\sigma^3 \tag{73}$$

$$\frac{4\pi\mu^2 g^2}{h^2} g_i g_j S_{ij,k}^{ei}(\sigma) = \frac{1}{c} g_k S_{k,ij}^{abs}(\sigma), \tag{74}$$

Assuming a Maxwell-Boltzmann distribution at T_{rel} for the relative velocity distribution function enables to write the emission and absorption coefficients as:

$$\eta_{\sigma,fb} = 2hc^2\sigma^3 \sum_{ijk} \frac{n_i^A n_j^B}{\xi(\mu, T_{rel})} \frac{g_k}{g_i g_j} h\sigma S_{k,ij}^{abs}(\sigma) \exp\left(\frac{E_i^A + E_j^B - E_k^{AB} - hc\sigma}{kT_{rel}}\right) \tag{75}$$

$$\kappa_{\sigma,fb} = \sum_{ijk} h\sigma S_{k,ij}^{abs}(\sigma) \, n_k^{AB} \left[1 - \frac{g_k}{g_i g_j} \frac{n_i^A n_j^B}{\xi(\mu, T_{rel}) n_k^{AB}} \exp\left(\frac{E_i^A + E_j^B - E_k^{AB} - hc\sigma}{kT_{rel}}\right)\right], \tag{76}$$

where g_i is the degeneracy of level i and $\xi(\mu, T_{rel})$ is the volumetric translational partition function of a particle of mass μ at temperature T_{rel}

$$\xi(\mu, T_{rel}) = \left(\frac{2\pi\mu k T_{rel}}{h^2}\right)^{\frac{3}{2}}. \tag{77}$$

Similarly to bound-bound transitions, the exact treatment of bound-free transitions in nonequilibrium requires to know detailed level-to-level cross sections, which are not always available. We detail in the following the status for the different bound-free mecanisms.

2.2.1 Atomic photoionization

The atomic photoionisation corresponds to :

$$A(k) + hc\sigma \rightarrow A^{+}(i) + e \tag{78}$$

The TOPBASE database [20] provides the absorption cross sections $\mathfrak{S}_k$ from levels up to a principal quantum number equal to 10 or 11 as a function of photon wavenumber. These cross sections correspond to:

$$\mathfrak{S}_k(\sigma) = h\sigma \sum_{ij} S^{abs}_{k,ij} \tag{79}$$

where j corresponds to the double degenerate unique internal energy level of the electron. In the two-temperature model, Eqs. 75, 76 and 79 lead to express the emission and absorption coefficients as :

$$\eta_\sigma = 2hc^2\sigma^3 \exp\left(-\frac{hc\sigma}{kT_{ve}}\right) \frac{n_{\rm at}}{Q_{\rm at}} \chi^{\rm neq} \sum_k g_k \exp\left(-\frac{E^{\rm at}_k}{kT_{ve}}\right) \mathfrak{S}_k(\sigma) \tag{80}$$

$$\kappa_\sigma = \frac{n_{\rm at}}{Q_{\rm at}} \left[\sum_k g_k \exp\left(-\frac{E^{\rm at}_k}{kT_{ve}}\right) \mathfrak{S}_k(\sigma)\right] \left[1 - \chi^{\rm neq} \exp\left(-\frac{hc\sigma}{kT_{ve}}\right)\right] \tag{81}$$

$$\chi^{\rm neq} = \frac{n_{\rm ion} n_{e-}}{n_{\rm at}} \frac{Q_{\rm at}}{2Q_{\rm ion}\xi(m_e, T_{ve})} \exp\left(\frac{E_{\rm ion}}{kT_{ve}}\right). \tag{82}$$

where $n_{\rm at}$, $n_{\rm ion}$, and $n_{\rm e-}$ are the total populations of respectively the atom, the produced ion and electron, $Q_{\rm at}$ and $Q_{\rm ion}$ are the atom and ion partition functions and m_e is the electron mass. $E_{\rm ion}$ is the ionization energy corrected from the Debye ionization lowering.
The factor $\chi^{\rm neq}$ characterizes the deviation from equilibrium and consequently from Kirchhoff's law.

2.2.2 Molecular photodissociation

We have included in the database the Schumann-Runge continuum:

$$O_2(k) + hc\sigma \rightarrow O(i) + O(j) \tag{83}$$

The thermal absorption cross sections for Schumann-Runge continuum are available in the temperature range 300-10000K and the wavenumber range 48000-77000 $\rm cm^{-1}$ [68, 69]. Since to our knowledge no detailed level-to-level absorption cross sections are available, we need to make some assumptions to deduce the absorption and emission coefficient in the framework of the two-temperatures model [70]. If we assume that the oxygen atoms are only produced in the ^{3}P and ^{1}D term of the oxygen ground configuration which corresponds to the asymptote state of the O_2 $B^3\Sigma^-_u$ electronic state, the thermal cross section can be written as:

$$\mathfrak{S}^{\rm LTE}(\sigma, T) = \frac{h\sigma}{Q_{O_2}(T)} \sum_k g_k \exp\left(-\frac{E^{O_2}_k}{kT}\right) \mathcal{S}^{abs}_{k,i_0 j_0}(\sigma) \tag{84}$$

where i_0 and j_0 represent the ^3P and ^1D terms of atomic oxygen and $Q_{O_2}(T)$ is the internal partition function of O_2. This equation combined to Eqs. 75 and 76 allows us to deduced the

spontaneous and induced emission coefficients in the two-temperatures model:

$$\eta_\sigma = 2hc^2\sigma^3 \exp\left(-\frac{hc\sigma}{kT_{rot}}\right) \mathfrak{S}^{\mathrm{LTE}}(\sigma, T_{rot}) n_{O_2} \chi^{\mathrm{neq}} \tag{85}$$

$$\kappa_\sigma^{ei} = \chi^{\mathrm{neq}} n_{O_2} \mathfrak{S}^{\mathrm{LTE}}(\sigma, T_{rot}) \exp\left(-\frac{hc\sigma}{kT_{rot}}\right) \tag{86}$$

$$\chi^{\mathrm{neq}} = \frac{n_O^2}{n_{O_2}} \frac{Q_{O_2}(T_{rot})}{Q_O^2(T_{ve})\xi(m_O, T_{rot})} \exp\left(\frac{E_{\mathrm{diss}} + E_{^1D}^O}{kT_{rot}} - \frac{E_{^1D}^O}{kT_{ve}}\right). \tag{87}$$

where n_O and n_{O_2} are the atomic and molecular oxygen total populations, E_{diss} the dissociation energy of the ground electronic state of O_2, and $E_{^1D}^O$ the energy of the ^1D term of atomic oxygen. The true absorption coefficient is approximated by:

$$\kappa_\sigma^{abs} = n_{O_2} \mathfrak{S}^{\mathrm{LTE}}(\sigma, T_{ve}) \tag{88}$$

χ^{neq} in the above equations deviates from unity in chemical nonequilibrium which leads to a deviation from Kirchhoff's law.

2.2.3 Molecular photoionization

Most of the available data for this mechanism correspond to room temperature. As its contribution remains small in the considered applications, we use pragmatically the room temperature cross sections Σ for O_2, N_2, CO, C_2 and CN [71, 72] and evaluate the absorption coefficient at equilibrium as:

$$\kappa_\sigma = N_{mol}(T)\Sigma \left[1 - \exp\left(-\frac{hc}{kT}\sigma\right)\right] \tag{89}$$

For the two-temperatures model, we use Eq. 89 and the Kirchhoff's law at T_{ve} to estimate the emission coefficient.

2.2.4 Photodetachment

The photodetachment of N^-, O^-, C^- which is described by:

$$A^- + hc\sigma \rightarrow A + e \tag{90}$$

is far to be fully understood. The available theoretical and experimental data show a certain scatter. According to the literature, the major contributions correspond to the photodetachment from the ^{3}P term of the ground configuration of N^-, from the ^{2}P term for O^- and from the ^{4}S term for C^-. The absorption coefficient has been expressed as:

$$\kappa_\sigma = [N_i \Sigma_i] \left[1 - \exp\left(-\frac{hc}{kT}\sigma\right)\right], \tag{91}$$

where N_i, the population of the above identified level of the negative ion, is estimated through a Saha equation from neutral atom and free electron populations and a temperature equal to T for the equilibrium situation and to T_{ve} for the two-temperatures model. The cross sections Σ_i have been obtained by averaging available data for N^- and O^- [10] and from calculations for C^- [73]. The associated emission coefficients are calculated using the Kirchhoff's law.

2.3 Free-free transitions

The free-free emission (Bremsstrahlung emission) is observed when an electron is slowed down by a collision with an ion, atom or molecule. The energy of the emitted photon is equal to the loss of kinetic energy. The cross section of the process depends on the relative velocity of colliders which can be taken equal to the electron velocity. As the electron velocities are assumed to follow a Maxwell-Boltzmann distribution at T_e, the bremsstrahlung emission coefficient and the inverse bremsstrahlung absorption coefficient are linked by the Kirchhoff's law (Eq. 4) with a Planck's function (Eq. 5) at T_e.

2.3.1 Electron-ion interaction

The free-free transitions in the field of ions are taken into account through the classical Kramers formula [74] corrected by a Gaunt factor $g(\sigma, T_e)$:

$$\eta_\sigma = g(\sigma, T_e)\frac{8}{3}\left(\frac{2\pi}{3kTm_e}\right)^{\frac{1}{2}}\frac{\alpha^2 e^6}{m_e c^3}\exp\left(-\frac{hc}{kT_e}\sigma\right)N_e N_i \tag{92}$$

where N_e and N_i are the densities of electrons and ions respectively, m_e is the electron mass, α is the ion charge and $e = \frac{q_e}{\sqrt{4\pi\epsilon_0}}$.
The Gaunt factors of Stallcop and Billman [75] have been used above 11604 K, those of Menzel and Pekeris [76] below 11604 K.

2.3.2 Electron-atom interaction

For free-free transitions involving atoms, we used for O and N the calculated inverse Bremsstrahlung cross sections $Q_a(\sigma, T_e)$ of Mjolsness and Ruppel [77] who give an analytical representation of their Hartee-Fock calculation for the temperature range 4000-12000 K and the wave number range 4800-24000 cm^{-1}, and for C the ones of Geltman [78] which cover the temperature range 500-20000 K and the wavenumber range 1000-20000 cm^{-1}. The absorption coefficient is given by:

$$\kappa_\sigma = [Q_a(\sigma, T_e)N_e N_{at}]\left[1 - \exp\left(-\frac{hc}{kT_e}\sigma\right)\right], \tag{93}$$

where N_e and N_{at} are the electron and atom densities.

2.3.3 Electron-diatom interaction

Free-free transitions have been included for N_2 and O_2 using the cross sections of Kivel [79] which cover the temperature range 3000-15000 K and the wavelength range 0.3-4.8 μm. These cross sections have been extrapolated below 3000 K and below 2083 cm^{-1}. The absorption coefficient is given by a relation similar to Eq. 93.

The total absorption coefficient due to bound-free and free-free transitions for an atmospheric air plasma is presented on Fig. 10 for two temperatures, 2000 K and 15000 K. The contributions of the different processes are presented. The preponderant contributive radiative processes are indicated.

2.4 Validation

An effort has been made to validate the selected and calculated data by systematically comparing the results with available measurements or predictions. The comparisons have been made when

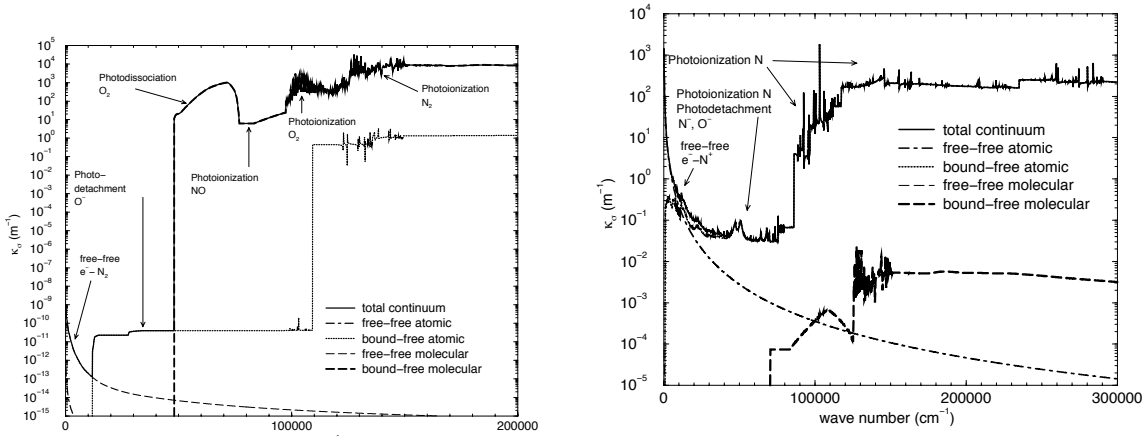

Figure 10: Continuum absorption for an atmospheric air plasma at 2000 K (left) and 15000 K (right) [10].

possible for a given process (radiative lifetimes for diatomic electronic systems for example) and also for more global data [9, 10, 11, 12].

For plasmas at local thermodynamic and chemical equilibrium, energy level populations are calculted from Boltzmann distribution and the chemical composition from the general equilibrium laws (Guldberg-Waage equation for dissociation and Saha equation for ionization), and from perfect gas law and electro-neutrality. The calculations of the required partition functions at LTE or for a multi-temperature thermodynamic state are described in [54].

Figure 11 presents for an LTE air plasma at 1 atm the optically thin source strength defined as:

$$S_R = \int_{\sigma 1}^{\sigma 2} \kappa_\sigma I^0_\sigma(T)\, d\sigma. \tag{94}$$

σ_1 and σ_2 correspond the experimental cutoff wave numbers. Our calculated source strength corresponds to cutoff wave numbers of 1000 cm^{-1} and 50000 cm^{-1} respectively. These values correspond to the different experimental cutoffs, except the ones of Nerem and Devoto for which σ_2 is equal to 58820 cm^{-1}. An overall good agreement is observed up to 14000K.

Spectral comparison has been made with the emission data obtained by Laux [80] with an ICP torch working with air at atmospheric pressure. Figure 12 presents the experimental and calculated absolute emission intensity along a diameter of the plasma torch. The temperature is about 7600 K at the center. It must be noted that a small background has to be removed from the experimental spectrum [5]. Differences in the UV NO bands can also be observed, but the overall agreement is good, especially with the latest measurements given in Ref. [5].

These comparisons between experiments and predictions in the equilibrium regime are also relevant because the problems of nonequilibrium chemistry and non-Boltzmann state-populations do not add complexity in the theoretical modelling.

Unfortunately such data were not available for CO_2 plasmas. We have thus developed an emission experimental set-up based on a 5 KW microwave torch at atmospheric pressure [86]. The emission spectra of CO_2 and $CO_2(97\%)$-$N_2(3\%)$ have been recorded. An Abel inversion procedure allows to deduced local emissivities. A careful analysis of the emission spectra in the UV and visible ranges has been performed and has shown that the plasma is at local thermodynamic equilibrium for molecules with a slight depletion of observed atomic levels. The predominant

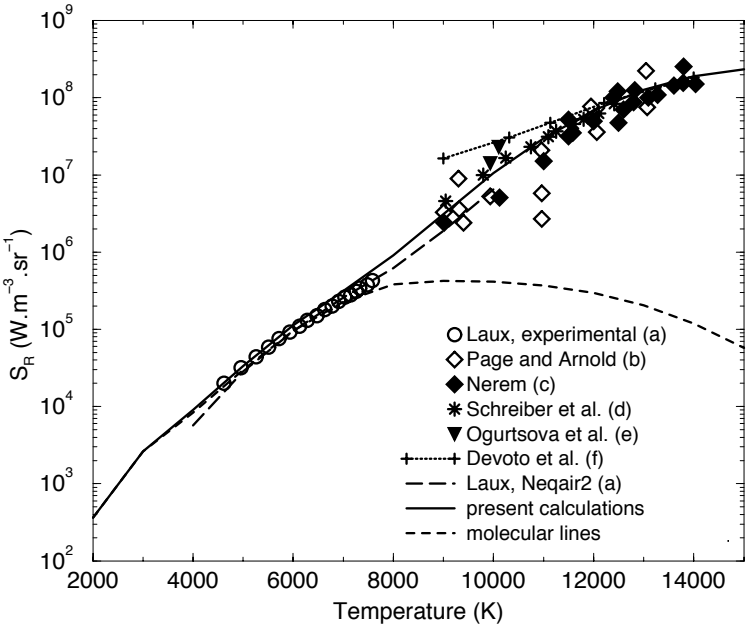

Figure 11: Optically thin emission of air plasmas at atmospheric pressure in the spectral range 1000 – 50000 cm^{-1}. Comparison between our calculations and available experimental or numerical data. a: [80], b: [81], c: [82], d: [83], e: [84], f: [85].

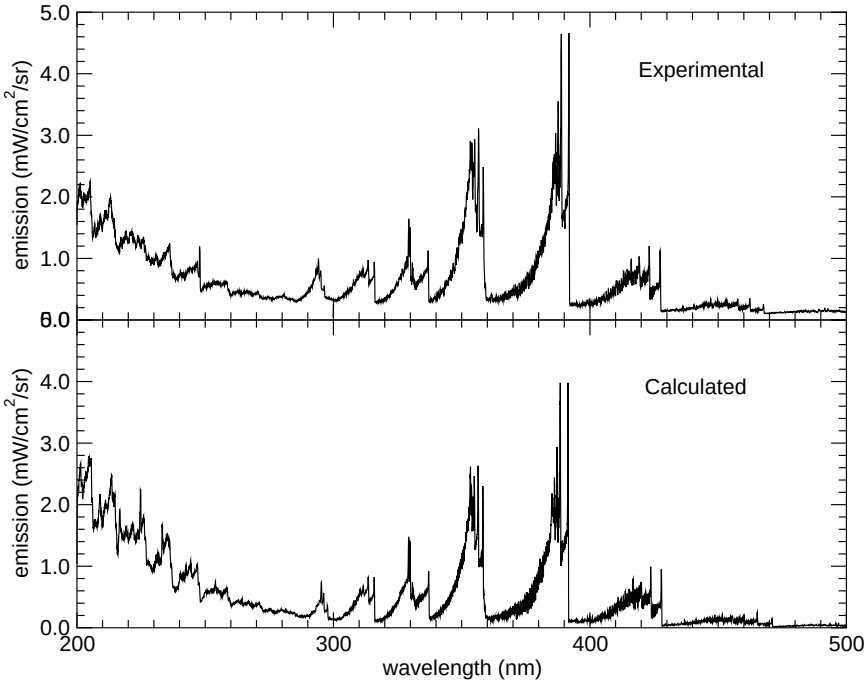

Figure 12: Comparison between experimental [80] and calculated emission intensity along a diameter of the air plasma torch.

observed systems are CN violet, CN red, and C_2 Swan. Significant contributions are also found from O_2, CO^+ and NO systems. Figure 13 presents a comparison between measured and calculated emissivities at the center of the CO_2(97%)-N_2(3%) plasma. The molecular temperature at the center of the plasma is about 5500K. For the pure CO2 plasma, it raises to about 6500K.

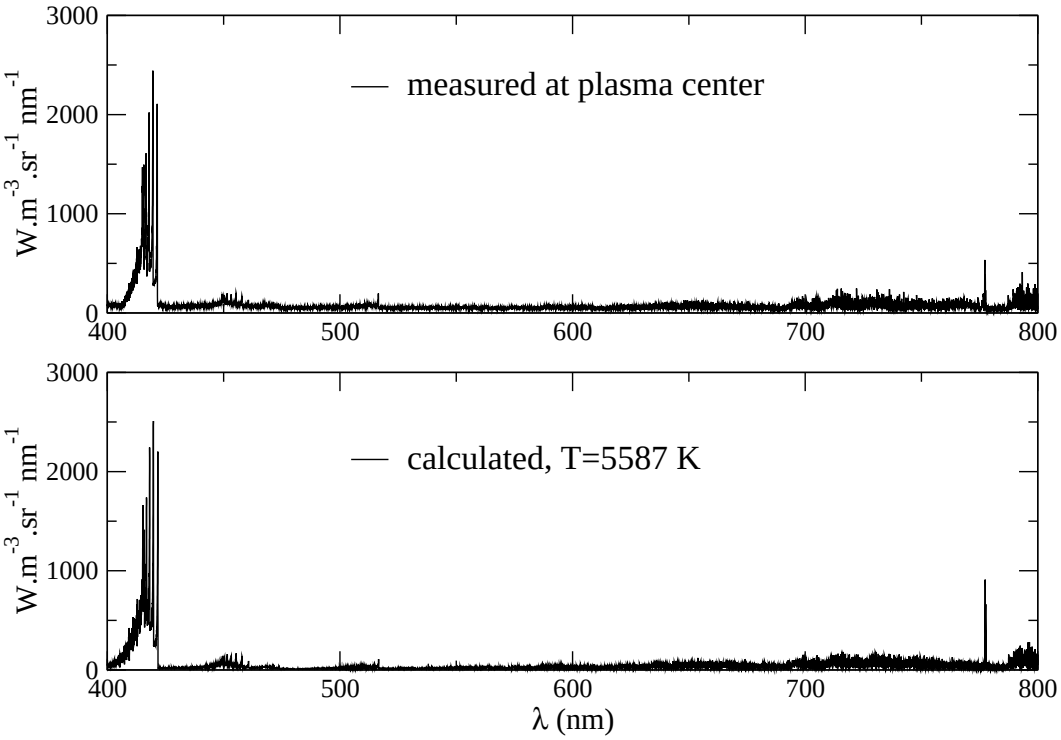

Figure 13: Comparison between measured and calculated absolute emissivities at the center of the atmospheric CO2(97%)-N3(3%) plasma (from [86]).

Figure 14 presents, in a spectral range centered on the CN red system, the experimental spectrum and the best adjustment. A systematic study of the sensitivity to the temperature has been carried out by calculating the root mean square error. Its evolution with the temperature is given in the insert of Fig. 14.

2.5 Contributions of the various mechanisms at equilibrium

We analyse in this section the relative contributions of the various emission mechanisms to total radiation at different temperatures for air and CO_2/N_2 plasmas. We limit our discussion to media at chemical and thermal equilibrium at temperature T and at atmospheric pressure. The optically thin emission strength $S_R = \int_{\sigma 1}^{\sigma 2} \kappa_\sigma I^0_\sigma(T)\, d\sigma$ is shown on Figs. 15 and 16 for air plasmas (79% N_2, 21% O_2) as a function of temperature. S_R is limited in Fig. 15 to the spectral range σ_1=1000 cm^{-1} – σ_2=50000 cm^{-1}, easily accessible experimentally, while the emission shown on Fig. 16 includes the vacuum UV contribution up to σ_2=150000 cm^{-1}. It is shown that the emission is dominated by diatomic line radiation below 6000 K and by atomic lines above 8000 K. Continuum contribution to the optically thin radiation seems to be relatively small. However, the predominance of VUV atomic lines at high temperature is generally damped in

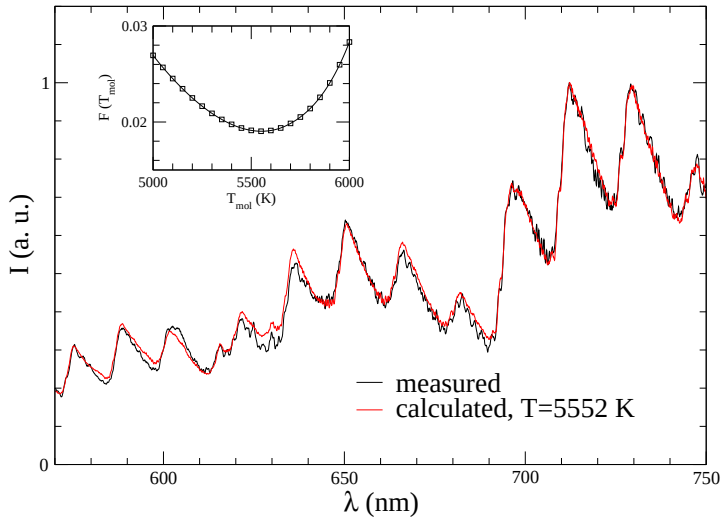

Figure 14: Comparison between measured and calculated emissivities fro the Δv=3, 4 and 5 bands of the CN red system at the center of the atmospheric CO_2(97%)-N_2(3%) plasma. (from [86]).

real applications due to the strong self-absorption of these lines. The continuum radiation is then no longer negligible. To outline the effects of absorption, we plot on figure 17 the total plasma emission, as corrected from self-absorption over a characteristic distance R:

$$S_R^{abs}(R) = \int_0^\infty \kappa_\sigma I_\sigma^0(T)\, \exp(-\kappa_\sigma R)\, d\sigma, \tag{95}$$

for various values of R. At 15000 K for instance, the emission is reduced by one order of magnitude for R as small as 1 mm.

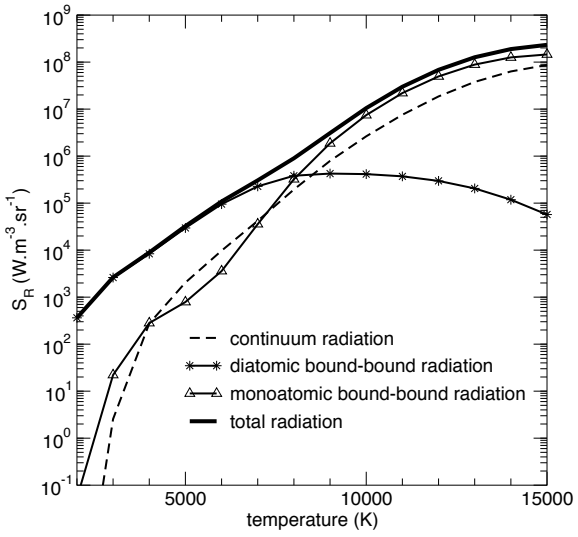

Figure 15: Optically thin emission of air plasmas at equilibrium at atmospheric pressure between 1000 and 50000 cm^{-1}.

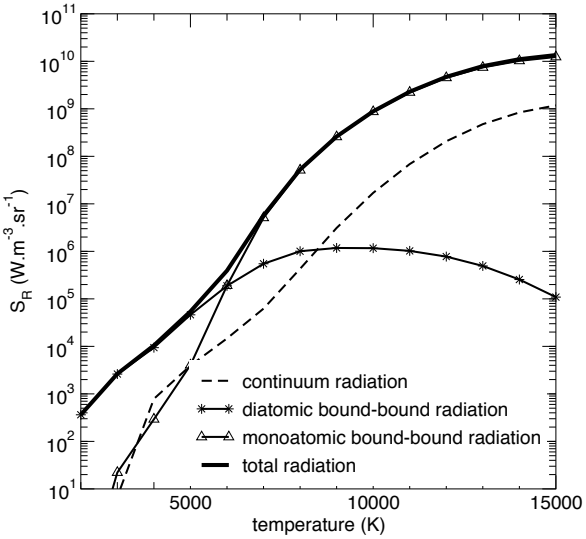

Figure 16: Optically thin emission of air plasmas at equilibrium at atmospheric pressure between 1000 and 150000 cm^{-1}.

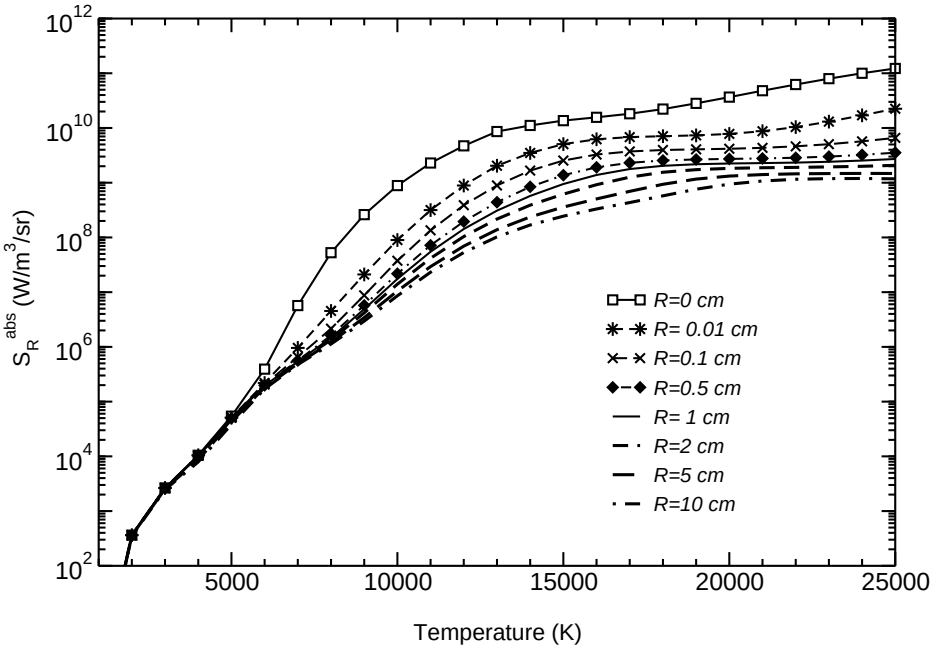

Figure 17: Volumetric emission of air plasmas at atmospheric pressure corrected from self-absorption on a characteristic distance R.

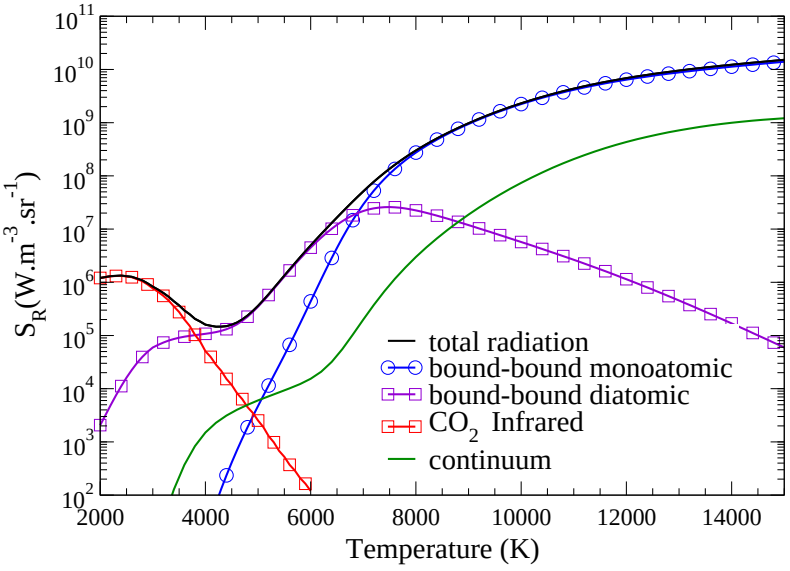

Figure 18: Contributions of CO_2 IR bands, diatomic bound-bound, atomic bound-bound, and continuum radiation to the optically thin emission of CO_2 (97%)-N_2 (3%) plasma at atmospheric pressure (adapted from Ref. [12]).

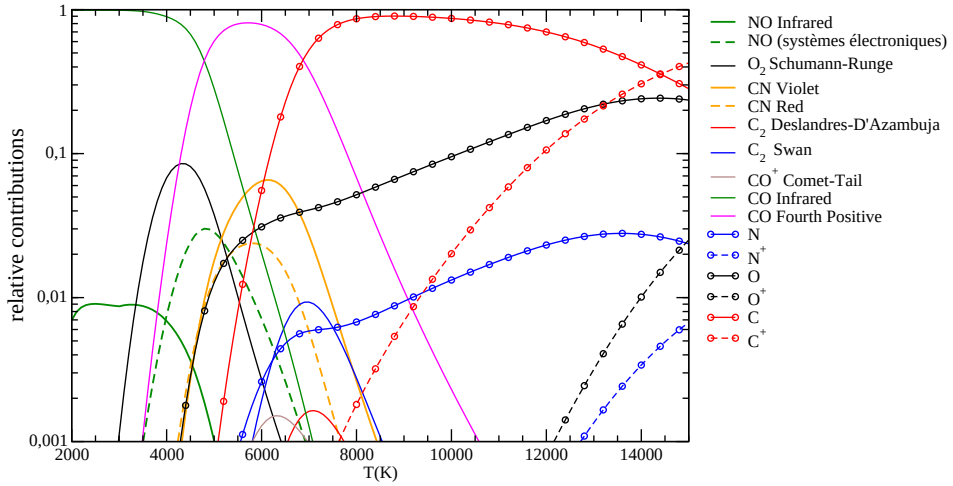

Figure 19: Details of the relative contributions of diatomic and atomic bound-bound radiation to the optically thin emission of CO_2 (97%)-N_2 (3%) plasma at atmospheric pressure (adapted from Ref. [12]).

For CO_2(97%)–N_2(3%) mixtures at atmospheric pressure, Figure 18 shows that the total optically thin emission iis first dominated by CO_2 infrared radiation (mostly the ν_3 bands near 4.3 μm) below 4000 K, then by diatomic line radiation between 4500 and 6500 K, and finally by atomic line radiation for higher temperatures. Here also, continuum radiation seems to be quite weak, but VUV atomic lines are very intense and are strongly self-absorbed in practical applications. The detailed contributions of diatomic and atomic bound-bound transitions are shown separately (without CO_2 radiation) in Fig. 19. At low temperature, CO infrared system is the most contributing, followed by CO fourth positive system between 4500 and 6500 K, and then by carbon atomic lines. It should be noted however that CO IR and fourth positive systems are likely to be strongly self-absorbed in practical applications as discussed in Sec. 3.2.

3 Application to earth and Mars entries

In addition to the spectroscopic properties described in the first part of this paper, the computation of radiative fluxes in entry applications requires the knowledge of the entire fields of population densities of the emitting states of each species. For molecules for instance, the populations of all electronic, vibrational, and rotational levels are required. The populations are generally calculated by neglecting the interaction with radiation field or by using approximate escape factors in some collisional-radiative models. The third part of the problem concerns the solution of radiative transfer problem including spatial, directional and spectral integrations.

We have combined our spectroscopic data and raditive transfer solvers with the aero-thermochemical fields predicted by other groups to compute wall radiative fluxes and volumetric radiative powers in some Earth and Mars entry applications.

3.1 Earth entry

The most widely considered data for radiation model validation are from the FireII flight experiment [87]. The database has been used to calculate the radiative intensities at the stagnation point for 4 points of Fire II re-entry trajectory [88]. The aerothermal fields used to calculate the different spectra are those of Ref. [89]. They have been computed using the chemical kinetic model of Park and a two-temperature model: T_{rot} for the translation of heavy particles and diatomic molecule rotation, T_v for diatomic vibration. We assume that electronic levels and free electrons are in equilibrium at T_v, which is written T_{ve} in the following. Figures 20 and 21 gives the temperatures and concentration fields along the stagnation line for the the flight time 1642.66 s.

Figure 22 shows the emission and absorption coefficients in the shock layer for FireII flight time

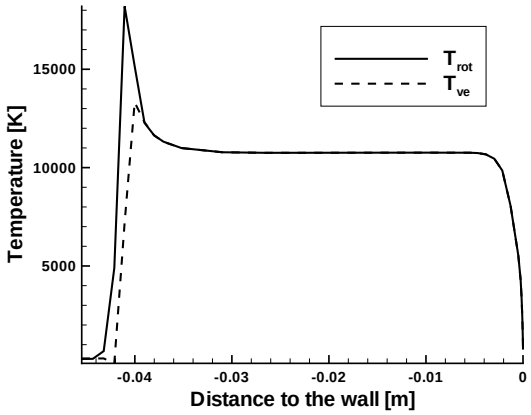

Figure 20: Temperature fields along the stagnation line for the trajectory point 1642.66 s (from [89]).

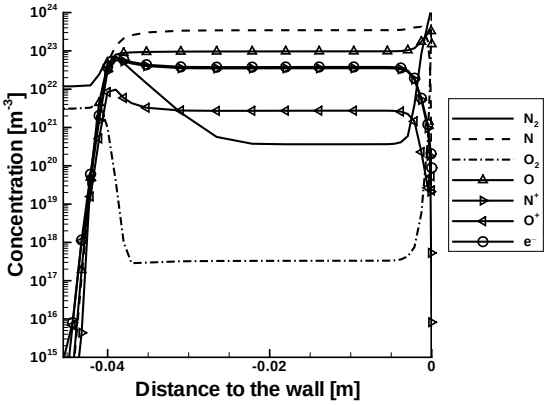

Figure 21: Concentration fields along the stagnation line for the same trajectory point (from [89]).

1642.66 s which corresponds to the maximum radiative heating. The most important mechanisms correspond to atomic lines in near IR and VUV regions, N_2 VUV systems, N_2^+ systems, and photoionization. The contribution of VUV represents 50% of the total incident intensity at the wall. It can also be seen that absorption must be taken into account in the visible range and especially in the VUV range. Neglecting absorption in the calculation leads to an overestimation of the incident flux by a factor of 55.

Our calculations show a good agreement with the data of the two radiometers (0.3– 0.6 μm and 0.2–4 μm) for the trajectory points 1642.66 s and 1637.5 s. The calculations overpredict the radiative intensities for the trajectory points 1634 s and 1648 s. Figure 23 compares the measured spectral intensity with our calculations for the trajectory point 1648 s. A few molecular systems can be identified (an experimental calibration problem explains the shift). Inverse photodetachment is found to contribute significantly in our calculations. This suggests to reexamine the modelling of this process to decrease the associated uncertainties.

Finally, figure 24 presents the cumulated flux incident on the wall for the trajectory point 1642.66 s. It points out the necessity to take into account the effect of chemical non-equilibrium on O_2 inverse photodissociation

3.2 Mars entry

As there are no direct experimental data for Mars entries, calculations have been carried out in the framework of testcase TC3 of the ESA/CNES radiation working group to simulate radiative

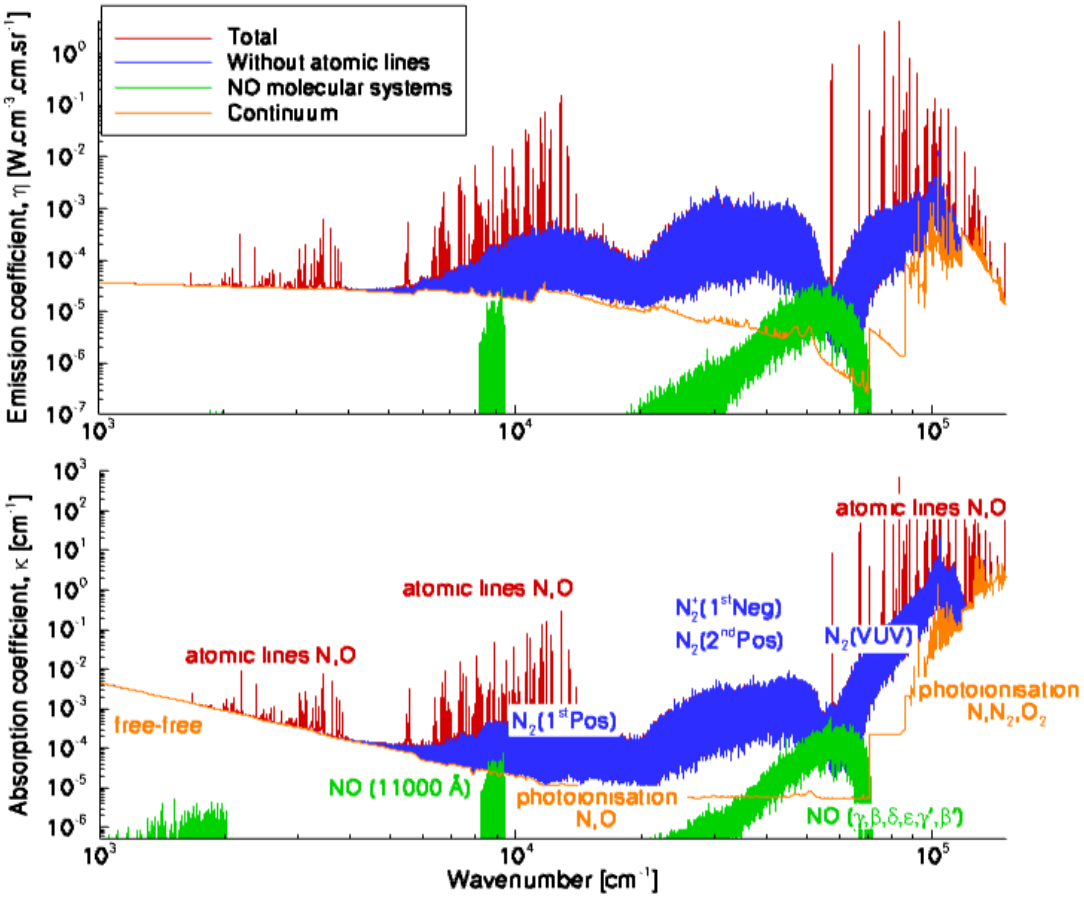

Figure 22: Spectral emission and absorption coefficients for a point in the shock layer (T_{rot}=16700 K and T_{ve}=10250 K). Flight time 1642.66 s (from [70]).

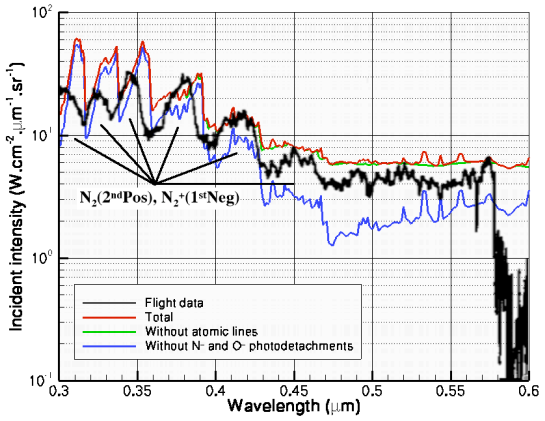

Figure 23: Spectral incident intensity on the stagnation point for the trajectory flight time 1648 s (from [88]).

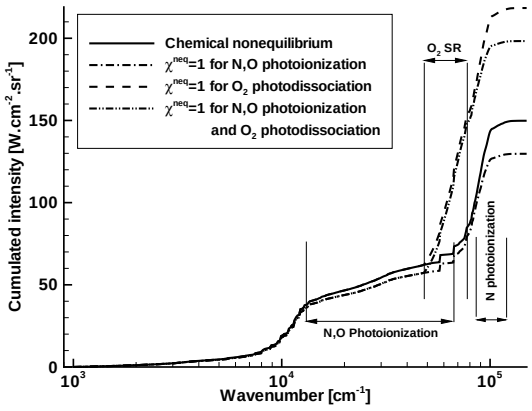

Figure 24: Cumulated incident intensity on the wall stagnation point for the trajectory time 1642.66 s (from [70]).

fluxes in the forebody and in the rear region of an axially symmetric vehicle [90, 91].

Different aerothermal fields, assuming local thermal equilibrium were provided for this test-case. Figure 25 shows for instance the multidomain temperature field around the vehicle assuming a pure CO_2 atmosphere. We carried out line by line calculations of the incident flux on different points of the vehicle. Some results for the forebody region are shown in Fig. 26 and the computed fluxes in the rear region are presented later as an application of statistical narrow-band models.

One of the most important conclusion of these calculations was that the incident flux is dominated by infrared radiation (mostly from CO_2) even for the stagnation line where the temperature exceeds 6000 K in the shock layer. Figure 26 shows indeed that the intense emission due to the CO fourth positive sytem in the VUV is strongly self absorbed. Its dominant contribution to the optically thin emission of CO_2 and CO_2/N_2 plasmas in the considered temperature range (see e.g. Figs. 18 and 19) is thus strongly attenuated by self-absorption. This result also outlines the need of validation of CO_2 spectroscopic databases above 3000 K.

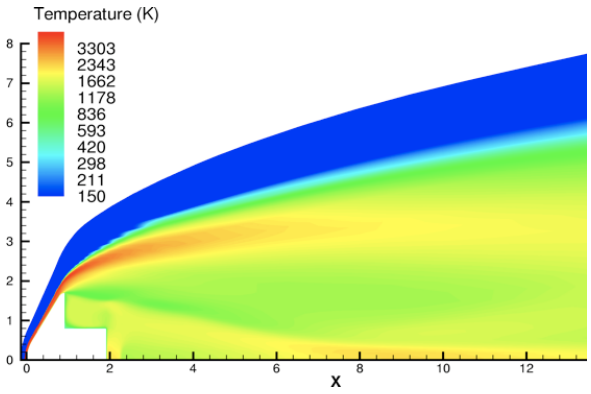

Figure 25: Prescribed temperature field around the simulated vehicle entering Mars atmosphere [90].

4 Approximate models

The use of a line by line calculations to perform 2D or 3D radiative transfer computations is very costly since it requires to solve the radiative transfer equation (eq. 1) with a sufficiently fine spectral resolution to correctly describe the transport of radiation in the fine structures of the spectra, namely in lines. This motivates the development of approximate models which do not have the high resolution structures but provide accurate predictions. Over the past few decades, such models have been developed to study infrared radiative transfer [92] generally for combustion applications or atmospheric propagation. However for higher temperatures, such developments are scarce [93] and to our knowledge there is no model able to correctly predict radiative transfer (emission and absorption) in a non-equilibrium plasma. We present here a model specific for high temperature-low pressure applications at thermal equilibrium which has been developed to estimate the flux in the wake of a an axially symmetric body entering Martian atmosphere [90].

4.1 Statistical Narrow-Band calculations for CO_2-CO mixtures

The Statistical Narrow band model of Mayer and Goody [94] has been used to model the infrared radiative properties of CO-CO_2 mixtures between 500 and 5000 cm^{-1}. The model assumes

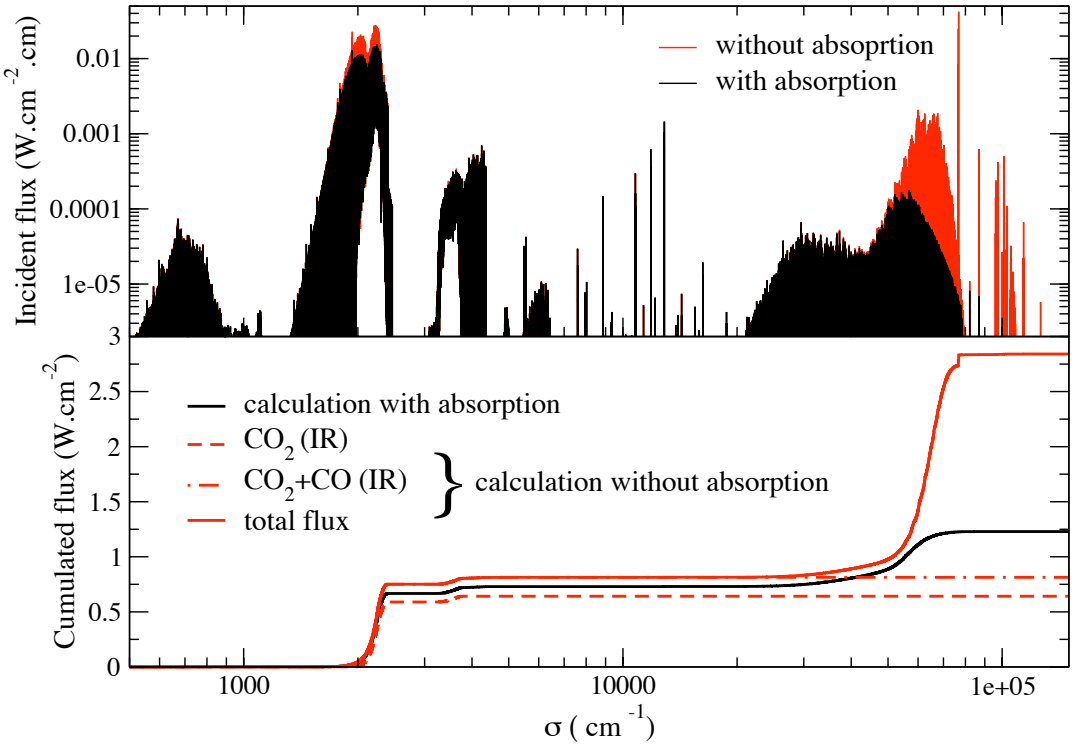

Figure 26: Spectral distribution of the incident radiative flux on the stagnation point of the MSRO simulation (testcase TC3 of the ESA/CNES radiation working group [91]).

random line positions. The transmissivity of a uniform column of length ℓ, averaged over a spectral band of width $\Delta\sigma$ is expressed as:

$$\overline{\tau_\sigma} = \frac{1}{\Delta\sigma}\int_{\Delta\sigma} \exp(-\kappa_\sigma \ell)\mathrm{d}\sigma = \exp\left(-\frac{\overline{W}}{\delta}\right), \tag{96}$$

where $\delta = \Delta\sigma/N$ is the mean spacing between the N absorption lines located in $\Delta\sigma$ and $\overline{W}$ is the mean black equivalent width of these lines defined by :

$$\overline{W} = \frac{1}{N}\sum_{\text{lines } i}\int_{-\infty}^{+\infty}\left[1-\exp\left(-\kappa_\sigma^i \ell\right)\right]\mathrm{d}\sigma. \tag{97}$$

where κ_σ^i is the absorption coefficient of line i.
For the considered application, the temperature range was limited to 4000 K , and the pressure is of about 100 Pa. The line profile has been taken of Voigt type for line by line calculations but assumed in the model of Doppler type characterized by the half-width at half-maximum γ_D. Among the different line intensity distributions which have been tested the exponential distribution has been selected. It yields:

$$\frac{\overline{W}}{\delta} = \frac{\gamma_D}{\delta} E\left(\frac{(S/\delta)u}{\gamma_D/\delta}\right), \tag{98}$$

where u is the pathlength $p_a\ell$, p_a being the partial pressure of the absorbing gas and E(y) is defined by:

$$E(y) = \frac{1}{\sqrt{\pi}} \int_{-\infty}^{+\infty} \frac{y e^{-\xi^2}}{1 + y e^{-\xi^2}} \mathrm{d}\xi. \tag{99}$$

The expression 98 introduces two parameters S/δ and γ_D/δ which have been determined in narrow bands, 25 cm^{-1} wide, as a function of the temperature for each molecule. S/δ corresponds to the mean absorption coefficient divided by p_a in the weak absorption limit. γ_D/δ is adjusted by fitting the curve of growth of $\overline{W}/\delta$ versus u obtained from line by line calculations for optical paths between 5 Pa.m and 5000 Pa.m. We checked that the mixture transmissivity, averaged over $\Delta\sigma$, may be calculated, with an excellent accuracy, as the product of CO and CO_2 averaged transmissivities. A further approximation (Curtis-Godson approximation [92]) is required to compute the transmissivity of non-uniform columns.
The incident radiation intensity on the wall along a ray of total length L, averaged over$\Delta\sigma$, is given by:

$$\overline{I_\sigma}(L) = \int_0^L I_\sigma^0(T(s)) \frac{\partial}{\partial s} \overline{\tau_\sigma}(s, L) \mathrm{d}s \tag{100}$$

4.2 Incident radiative flux on a body entering Martian atmosphere

The IR incident radiative intensity has been calculated using line by line or the narrow-band model for the aerothermal fields presented in section 3.

A ray tracing method has been used to calculate the incident flux on different points of the vehicle wall with 900 discrete solid angles. Due to the low pressure, a discretization of 5 10^{-3} cm^{-1} has to be used for the line by line calculation which leads to solve around 600 000 times the RTE. The CPU time ratio between line by line and statistical narrow-band models is typically about 300. The good agreement between the two simulations is illustrated on Fig. 28. The third curve of this figure corresponds to the weak absorption limit and is equivalent to the use of a mean absorption coefficient or to the smeared rotational model. By neglecting the high resolution spectral correlations, this approximation leads to an overestimation of wall fluxes .

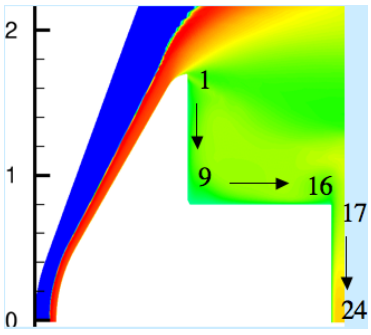

Figure 27: Calculation points of the incident intensity

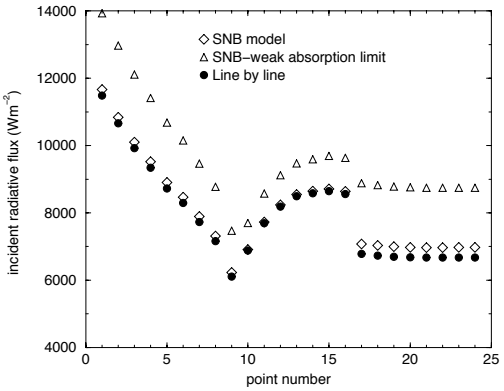

Figure 28: Comparaison between LBL calculations, full SNB results and SNB results using the weak absorption limit for the different basis points [90].

An approximate model, able to deal with optically thick systems of diatomic electronic states under nonequilibrium conditions, is under development. In the same manner, such model for

CO_2 under vibrational nonequilibrium conditions would be suitable for Mars entries.

Acknowledgements:
We warmly acknowledge the contributions of Sophie Chauveau, Christine Deron, Yacine Babou and Jean-Michel Lamet to this work. We are grateful to *Agence Nationale de la Recherche (ANR)*, ONERA, and to Schneider Electric S.A. for their support of this study, and to the *Institut du Développement et des Ressources en Informatique Scientifique (IDRIS)* for providing us with computational facilities.

References

[1] E.E. Whiting, C. Park, Y. Liu, J.O. Arnold, and J.A. Paterson. NEQAIR96, Nonequilibrium and Equilibrium Radiative Transport and Spectra Program: User's Manual. Reference Publication 1389, NASA, Ames Research Center, Moffet Field, California, Dec 1996.

[2] L.C. Hartung. Predicting radiative heat transfer in thermo-chemical non-equilibrium flow-fields: theory and user's manual for the LORAN code. Technical Memorandum 4564, NASA Langley Research Center, Hampton, VA 23681-0001, September 1994.

[3] K. Fujita and T. Abe. SPRADIAN, structural package for radiation analysis: theory and application. Technical report, ISAS Report No 669, 1997.

[4] L.A. Kuznetsova and S.T. Surzhikov. Absorption cross sections of diatomic molecules for problems of radiative heat transfer in low-temperature plasma. *High Temperature*, 37(3):374–385, 1999.

[5] C.O. Laux. Radiation and nonequilibrium collisinal-radiative models. In *VKI special course on physico-chemical models for high enthalpy and plasma flows modeling*, June, 4-7 2002.

[6] A. Smith, A. Wood, J. Dubois, M. Fertig, and B. Pfeiffer. Plasma radiation database parade v22 final report. Technical Paper 3, ESTEC contract11148/94/NL/FG, FGE TR28/96, Oct 2006.

[7] C.O. Johnston. *Nonequilibrium Shock-Layer Radiative Heating for Earth and Titan Entry.* PhD thesis, Virginia Polytechnic Institute and State University, Blacksburg, Virginia, November, 17 2006.

[8] P. Passarinho and M. Lino da Silva. GPRD, a database for the spectral properties of diatomic molecules of atmospheric interest. *Journal of Molecular Spectroscopy*, 236(1):148–149, 2006.

[9] S. Chauveau, M.-Y. Perrin, Ph. Rivière, and A. Soufiani. Contributions of diatomic molecular electronic systems to heated air radiation. *Journal of Quantitative Spectroscopy and Radiative Transfer*, 72:503–530, 2002.

[10] S. Chauveau, Ch. Deron, M.-Y. Perrin, Ph. Rivière, and A. Soufiani. Radiative transfer in LTE air plasmas for temperatures up to 15000 K. *Journal of Quantitative Spectroscopy and Radiative Transfer*, 77:113–130, 2003.

[11] Y. Babou. *Transferts radiatifs dans les plasmas de mélanges CO2/N2 : bases de données spectroscopiques, étude expérimentale et application aux rentrées atmosphériques.* PhD thesis, Université Paris Sud, July 2007.

[12] Y. Babou, Ph. Rivière, M. Y. Perrin, and A. Soufiani. Spectroscopic data for the prediction of radiative transfer in CO_2-N_2-O_2 plasmas. *J. Quant. Spectrosc. Radiat. Trannsfer*, in press, doi:10.1016/j.jqsrt.2008.09.007, 2008.

[13] M.Y. Perrin and A. Soufiani. Approximate radiative properties of methane at high temperature. *Journal of Quantitative Spectroscopy and Radiative Transfer*, 103:3–13, 2007.

[14] P. Rivière, S. Langlois, A. Soufiani, and J. Taine. An approximate database of H_2O infrared lines for high temperature applications at low resolution. Statistical narrow-band model parameters. *Journal of Quantitative Spectroscopy and Radiative Transfer*, 53(2):221–234, 1995.

[15] S. Chauveau. *Constitution de bases de données spectroscopiques relatives à un plasma d'air. Application au calcul de transferts radiatifs.* Thèse de doctorat, École Centrale Paris, 2001.

[16] W.C. Martin, J.R. Fuhr, D.E. Kelleher, A. Musgrove, J. Sugar, W.L. Wiese, P.J. Mohr, and K. Olsen. NIST Atomic Spectra Database (version 2.0). [Online] Available: http://physics.nist.gov/asd2 [March 31, 2005], Gaithersburg, MD, 1999.

[17] R. Hirata and T. Horaguchi. Atomic Spectral Line List (Hirata+ 1995). *VizieR Online Data Catalog*, page http://adsabs.harvard.edu/abs/1994yCat.6069, 1994.

[18] R.L. Kurucz and E. Peytremann. Sao special report 362. Technical report, NASA-CR-142879,142880,142881, 1975.

[19] R.L. Kelly. http://cfa-www.harvard.edu/ampcgi/kelly.pl.

[20] W. Cunto, C. Mendoza, F. Ochsenbein, and C. J. Zeippen. Topbase at the CDS. *Astronomy and Astrophysics*, 275:L5, 1993.

[21] The Opacity Project Team. *The Opacity Project*, volume 1. Institute of Physics Publishing, Bristol and Philadelphia, 1995.

[22] M.J. Seaton. Atomic data for opacity calculations: General description. *Journal of Physics B. Atomic and Molecular Physics*, 20:6363–6378, 1987.

[23] H.R. Griem. *Principles of plasma spectroscopy.* Cambridge University Press, 1997.

[24] N. Konjevic. Plasma broadening and shifting of non-hydrogenic spectral lines: present status and applications. *Physics Reports*, 316(6):339–401, 1999.

[25] H.R. Griem. *Plasma spectroscopy.* McGraw-Hill Book Company, New York, 1964.

[26] G. Traving. *Plasma Diagnostics*, chapter Interpretation of line broadening and line shift, pages 67–134. North-Holland, Amsterdam, 1968.

[27] Ph. Rivière. Systematic semi-classical calculations of stark broadening parameters of NI, OI, NII, OII multiplets for modelling the radiative transfer in atmospheric air mixture plasmas. *Journal of Quantitative Spectroscopy and Radiative Transfer*, 73:91–110, 2002.

[28] S. Sahal-Bréchot. Théorie de l'élargissement et du déplacement des raies spectrales sous l'effet des chocs avec les électrons et les ions dans l'approximation des impacts. *Astronomy & Astrophysics*, 2:322–354, 1969.

[29] S. Sahal-Bréchot. Théorie de l'élargissement et du déplacement des raies spectrales sous l'effet des chocs avec les électrons et les ions dans l'approximation des impacts. *Astronomy & Astrophysics*, 1:91–123, 1969.

[30] H.R. Griem. *Spectral line broadening by plasmas.* Academic Press, 1974.

[31] H. Lefebvre-Brion and R. W. Field. *Perturbations in the spectra of diatomic molecules.* Academic Press, London, 1986.

[32] J.M. Brown, E.A. Colbourn, J.K.G. Watson, and F.D. Wayne. An effective hamiltonian for diatomic molecules. *Journal of Molecular Spectroscopy*, 74:294–318, 1979.

[33] R.N. Zare, A.L. Schmeltejopf, W.J. Harrop, and D.L. Albritton. A direct approach for the reduction of diatomic spectra to molecular constants for the construction of RKR potentials. *Journal of Molecular Spectroscopy*, 46:37–66, 1973.

[34] P.H. Paul. Calculation of transition frequencies and rotational line strengths in the γ bands of nitric oxide. *Journal of Quantitative Spectroscopy and Radiative Transfer*, 57(5):581–589, 1997.

[35] E.E. Whiting, A. Schadee, J.B. Tatum, J.T. Hougen, and R.W. Nicholls. Recommended conventions for defining transition moments and intensity factors in diatomic molecular spectra. *Journal of Molecular Spectroscopy*, 80:249–256, 1980.

[36] R. Rydberg. Graphische darstellung einiger bandenspektroskopischer ergebnisse. *Zeitschrift für Physik*, 73:376–385, 1931.

[37] O. Klein. Zur berechnung von potentialkurven für zweiatomige moleküle mit hilfe von spektraltermen. *Zeitschrift für Physik*, 76:226–235, 1932.

[38] A.L. Rees. The calculation of the potential-energy curves from band-spectroscopy data. *Proceedings of the Physical Society*, A59:998–1008, 1947.

[39] H. M. Hulburt and J. O. Hirschfelder. Potential energy functions for diatomic molecules. *Journal of Chemical Physics*, 9:61–69, 1941.

[40] I. Kovacs. *Rotational structure in the spectra of diatomic molecules.* American Elsevier Publishing company INC, New York, 1969.

[41] G.D.T. Tejwani, B.M. Golden, and E.S. Yeung. Pressure-broadened linewidths of nitric oxide. *Journal of Chemical Physics*, 65(12):5110–5114, 1976.

[42] P.K. Falcone, R.K. Hanson, and C.H. Kruger. Tunable diode laser measurements of the band strength and collision halfwidths of nitric oxide. *Journal of Quantitative Spectroscopy and Radiative Transfer*, 29(3):205–221, 1983.

[43] J.M. Hartmann, L. Rosenmann, M.-Y. Perrin, and J. Taine. Accurate calculated tabulations of CO line broadening by H_2O, N_2, O_2, and CO_2 in the 200–3000 K temperature range. *Applied Optics*, 27(15):3063–3065, 1988.

[44] A.Y. Chang, M.D Di Rosa, and R.K. Hanson. Temperature dependence of collision broadening and shift in the NO $A \leftarrow X$ (0,0) band in the presence of argon and nitrogen. *Journal of Quantitative Spectroscopy and Radiative Transfer*, 47:375–390, 1992.

[45] R.G. Breene. Spectral line broadening in air molecule systems. *Applied Optics*, 6:141–147, 1967.

[46] H. Oertel, M. Kratzat, J. Imschweiler, and T. Noll. Fluorescence from $^1\Pi_u$ and $^1\Sigma_u^+$ states of molecular nitrogen excited with synchrotron radiation between 12.4 and 18.8 eV. *Chemical Physics Letters*, 82:552–556, 1981.

[47] A. Kam, J.R. Lawall, M.D. Lindsay, F.M. Pipkin, R.C. Short, and P. Zhao. Precise spectroscopy and lifetime measurement of electron-impact-excited N_2: the $c_4'^1\Sigma_u^+(v=3)$ Rydberg level. *Physical Review A*, 40(3):1279–1288, 1989.

[48] W. Ubachs, L. Tashiro, and R.N. Zare. Study of the N_2 $b^1\Pi_u$ state via 1+1 multiphoton ionization. *Chemical Physics*, 130:1–13, 1989.

[49] H. Helm, I. Hazell, and N. Bjerre. Lifetimes and Rydberg-valence state mixing of the c'$^1\Sigma_g^+(v=4)$and c $^1\Pi_u(v=4)$ states of N_2. *Physical Review A*, 48(4):2762–2771, 1993.

[50] W. Ubachs, K.S.E. Eikema, and W. Hogervorst. Narrow-band extreme ultraviolet laser radiation tunable in the range 90.5-95 nm. *Applied Physics B*, 57:411–416, 1993.

[51] C.W. Walter, P.C. Cosby, and H. Helm. Predissociation quantum yields of singlet nitrogen. *Physical Review A*, 50(4):2930–2936, 1994.

[52] J. Luque and D.R. Crosley. Radiative and predissociative rates for NO $A^2\Sigma^+$ $v' = 0-5$ and $D^2\Sigma^+$ $v' = 0-3$. *Journal of Chemical Physics*, 112(21):9411–9416, 2000.

[53] B.R. Lewis, L. Berzins, J.H. Carver, and S.T. Gibson. Rotational variation of predissociation linewidth in the Schumann-Runge bands of $^{16}O_2$. *Journal of Quantitative Spectroscopy and Radiative Transfer*, 36(3):187–207, 1986.

[54] Y. Babou, Ph. Rivière, M. Y. Perrin, and A. Soufiani. High-temperature and nonequilibrium partition function and thermodynamic data of diatomic molecules. *International Journal of Thermophysics*, in press, DOI 10.1007/s10765-007-0288-6, 2007.

[55] L. S. Rothman and et al. The hitran 2004 molecular spectroscopic database;. *Journal of Quantitative Spectroscopy and Radiative Transfer*, 96(2):139–204, 2005.

[56] L. S. Rothman, R. B. Wattson, R. Gamache, J. W. Schroeder, and A. McCann. HITRAN HAWKS and HITEMP: high-temperature molecular database. In J. C. Dainty, editor, *Proc. SPIE Vol. 2471, p. 105-111, Atmospheric Propagation and Remote Sensing IV*, volume 2471, pages 105–111, 1995.

[57] M. B. E. Aguir, M. Y. Perrin, and J. Taine. Variational calculation of energies of highly excited rovibrational states of $^{12}C^{16}O_2$. *Journal of Molecular Spectroscopy*, 215(2):234–243, 2002.

[58] S. A. Tashkun, V. I. Perevalov, J-L. Teffo, A. D. Bykov, and N. N. Lavrentieva. Cdsd-1000, the high-temperature carbon dioxide spectroscopic databank. *Journal of Quantitative Spectroscopy and Radiative Transfer*, 82(1-4):165–196, 2003.

[59] D. Scutaru, L. Rosenmann, and J. Taine. Approximate intensities of CO_2 hot bands at 2.7, 4.3, and 12μm for high temperature and medium resolution applications;. *Journal of Quantitative Spectroscopy and Radiative Transfer*, 52(6):765–781, 1994.

[60] L. Rosenmann, J. M. Hartmann, M. Y. Perrin, and J. Taine. Accurate calculated tabulations of IR and Raman CO_2 line broadening by CO_2, H_2O, N_2, O_2 in the 300–2400-K temperature range. *Applied Optics*, 27(18):3902–3906, 1988.

[61] B. A. Thompson, P. Harteck, and R. R. Reeves, Jr. Ultraviolet Absorption Coefficients of CO_2, CO, O_2 H_2O, N_2O, NH_3, NO, SO_2, and CH_4 between 1850 and 4000 . *Journal of Geophysical Research*, 68:6431–6436, 1963.

[62] W. H. Parkinson, J. Rufus, and K. Yoshino. Absolute absorption cross section measurements of CO_2 in the wavelength region 163-200 nm and the temperature dependence. *Chemical Physics*, 290(2-3):251–256, 2003.

[63] R. J. Jensen, R. D. Guettler, and J. L. Lyman. The ultraviolet absorption spectrum of hot carbon dioxide. *Chemical Physics Letters*, 277(4):356–360, 1997.

[64] Matthew A. Oehlschlaeger, David F. Davidson, Jay B. Jeffries, and Ronald K. Hanson. Ultraviolet absorption cross-sections of hot carbon dioxide. *Chemical Physics Letters*, 399(4-6):490–495, 2004.

[65] M. Slack and A. Grillo. High temperature rate coefficient measurements of CO + O chemiluminescence. *Combustion and Flame*, 59(2):189–196, 1985.

[66] A. Grillo and M. Slack. CO +O chemiluminescence - Rate coefficient and spectral distribution. In *Shock tubes and waves; Proceedings of the Thirteenth International Symposium, Niagara Falls, NY, July 6-9, 1981*, pages 576–584, (A83-26126 10-34) Albany, NY, 1982. State University of New York Press.

[67] D. Mihalas and B. Weibel-Mihalas. *Foundations of Radiation Hydrodynamics*. Dover Publications, INC, Mineloa, 1999.

[68] D.R. Churchill, B.H. Armstrong, R.R. Johnston, and K.G. Muller. Absorption coefficients of heated air: a tabulation to 24000K. *Journal of Quantitative Spectroscopy and Radiative Transfer*, 6:371–442, 1966.

[69] A. Kh. Mnatsakanyan. Photodissociation and photoionization of diatomic molecules at high temperatures. *Teplofizika Vysokikh Temperatur*, 6(2):236–241, 1966.

[70] J.M. Lamet, Y. Babou, Ph. Riviere, M.Y. Perrin, and A. Soufiani. Radiative transfer in gases under thermal and chemical nonequilibrium conditions: Application to earth atmospheric re-entry. *Journal of Quantitative Spectroscopy and Radiative Transfer*, 109:235–244, 2008.

[71] J.A. Fennely and D.G. Torr. Photoionization and photoabsorption cross sections of O, N_2, O_2, and N for aeronomic calculations. *Atomic data and nuclear data tables*, 51:321–363, 1992.

[72] G.S. Romanov, Yu. A. Stankevich, L.K. Stanchits, and K.L. Stepanov. Thermodynamic and optical properties of gases in a wide range of parameters. *International Journal of Heat and Mass Transfer*, 38(3):545–556, 1995.

[73] N. Miura, T. Noro, and F. Sasaki. Theoretical study of the $2s2p^4\,{}^4P$ resonance state in the photodetachment of C^-. *Journal of Physics B: Atomic and Molecular Physics*, 30(23):5419–5427, 1997.

[74] H.A. Kramers. *Philosophical Mag*, 46:836, 1923.

[75] J. R. Stallcop and K. W. Billman. Analytical formulae for the inverse bremsstrahlung absorption coefficient. *Plasma Physics*, 16(12):1187–1189, 1974.

[76] D. H. Menzel and C. L. Pekeris. Absorption coefficients and hydrogen line intensities. *Monthly Notices of the Royal Astronomical Society*, 96:77, 1935.

[77] R.C. Mjolsness and H.M. Ruppel. Contribution of inverse neutral bremsstrahlung to the absorption coefficient of heated air. *Journal of Quantitative Spectroscopy and Radiative Transfer*, 7:423–427, 1967.

[78] S. Geltman. Free-free radiation in electron-neutral atom collisions. *Journal of Quantitative Spectroscopy and Radiative Transfer*, 13:601–613, 1973.

[79] B. Kivel. Bremsstrahlung in air. *Journal of Quantitative Spectroscopy and Radiative Transfer*, 7:51–60, 1967.

[80] C.O. Laux. *Optical diagnostics and radiative emission of air plasma.* PhD thesis, High Temperature Gasdynamics Laboratory-Mechanical Engineering Department-Stanford University, report No. T-288, 1993.

[81] W.A. Page and J.O. Arnold. Shock layer radiation of blunt bodies traveling at reentry velocities; cited in Ref. [80]. *NASA TR-R193*, 1964.

[82] R.M. Nerem. Stagnation point heat transfer in high enthalpy gas flows; cited in Ref. [80]. *Wright Patterson Air Force Base, OH, TDR-64-11*, Flight Dynamics Lab, 1964.

[83] P.W. Schreiber, A.M. Hunter, and K.R. Benedetto. Electrical conductivity and total emission coefficient of air plasma. *American Institute of Aeronautics and Astronautics Journal*, 11(6):815–821, 1973.

[84] N.N. Ogurtsova, I.V. Podoshenskii, and V.M. Shelemina. The radiative power of air, N_2 and CO_2 at 10000K; cited in Ref. [80]. *Teplofizica Visokikh Temperatur*, 6:788–793, 1968.

[85] R.S. Devoto, U.H. Bauder, J. Cailleteau, and E. Shires. Air transport coefficient from electric arc measurements. *Phys. Fluids*, 21:552–558, 1978.

[86] Y. Babou, Ph. Rivière, M. Y. Perrin, and A. Soufiani. Spectroscopic study of microwave plasmas of CO_2 and CO_2-N_2 mixtures at atmospheric pressure. *Plasma Sources Science and Technology*, 17:045010(11p), 2008.

[87] D. Cauchon. Radiative heating results from the Fire II flight experiment at a reentry velocity of 11.4 kilometers per second. Technical Memorandum X-1402, NASA Langley Research Center, Hampton, VA 23681-0001, July 1967.

[88] J.M. Lamet, Y. Babou, Ph. Rivière, A. Soufiani, and M.-Y. Perrin. Radiative transfer in earth entry: application to the Fire II project experiment. In *Proceedings of the 2nd International Workshop on Radiation of High Temperature Gases in Atmospheric Entry*, Rome, Italy, September 2006.

[89] F. Mazoué and L. Marraffa. Determination of the radiation emission during the FIRE II entry. In *Proceedings of the 2nd International Workshop on Radiation of High Temperature Gases in Atmospheric Entry, Rome, 6-8 September*, 2006.

[90] Ph. Rivière, M.-Y. Perrin, and A. Soufiani. Line-by-line and statistical narrow-band calculations of radiative transfer in some atmospheric entry problems. In *Proceedings of the first international workshop on radiation of high temperature gases in atmospheric entry, Lisbon*, pages 189–196. ESA SP-533, 2003.

[91] Y. Babou, Ph. Rivière, M.-Y. Perrin, and A. Soufiani. Prediction of radiative flux distribution over the front shield of a vehicle entering Martian atmosphere- Contribution to test case TC3. In *Proceedings of the 2nd International Workshop on Radiation of High Temperature Gases in Atmospheric Entry*, Rome, Italy, September 2006.

[92] J. Taine and A. Soufiani. Gas IR radiative properties: from spectroscopic data to approximate models. *Advances in Heat Transfer*, 33:295–414, 1999.

[93] Ph. Rivière, A. Soufiani, M.Y. Perrin, H. Riad, and A. Gleizes. Air mixture radiative property modelling in the temperature range 10000-40000k. *Journal of Quantitative Spectroscopy and Radiative Transfer*, 56(1):29–45, 1996.

[94] R. Goody and Y. Young. *Atmospheric Radiation.* Oxford University Press, 1989.